Image Segmentation Applied to Volumetric Measurements on Centrifugal Microfluidic Platforms in Motion

Alexei Kazarine

Department of Chemistry

McGill University

Montreal, Quebec, Canada

December 15 2013

A thesis submitted to McGill University in partial fulfillment of the requirements of the degree of Master of Science

Abstract

Microfluidic platforms allow the implementation of classical analytical operations at a mere fraction of the time, cost and resources required conventionally while granting the potential for measurements to be taken directly in the field by untrained personnel. Centrifugal microfluidic (CM) platforms, a subset of microfluidic platforms, use centrifugal force to direct liquid flow and perform a variety of analytical operations.

Although the use of centrifugal force grants CM platforms many advantages such as a high degree of parallelism, the potential for portability, and the capability to pump liquids irrespective of their physicochemical properties, it creates a design paradigm that requires all platform operations to occur while the platform is in motion. Stopping a CM platform may result in unintended capillary induced flow in channels that can disrupt the intended operation and even cause a loss of sample.

In accordance with this paradigm, it is important to develop measurement techniques that can be utilized while CM platforms are in motion. One measurement of importance is the volume of liquid aliquots inside a CM platform. The capability to measure volume directly on CM platforms in motion could allow experiments to quantify liquid flow in real time and avoid the use of volume metering chambers, which occupy valuable platform space.

In this thesis, a new technique based on image segmentation was created to perform volume measurements on CM platforms in motion. Evaluation platforms containing a black contrast layer were fabricated and injected with liquid aliquots. High-resolution images of the evaluation platforms in motion were obtained with a high speed camera synchronized to a strobe light and the images were processed digitally. Platform images were then converted to an intensity space before image segmentation was applied to trace the inner contour of each liquid aliquot. The contour of each measured aliquot was filled and an area was computed. This area was ratioed against that obtained for a calibration volume located on the same image to obtain the volume of the aliquot.

The volume measurement technique was characterized through experiments designed to test its precision and accuracy over a range of volumes. The results were found to be 1 and 2% respectively. Further characterization of the technique revealed its flexibility in regards to optical magnification, chamber shape, size and aspect ratio and platform rotational frequency. An investigation into the effects of surface tension on the method precision was also conducted. The applicability of the technique to liquids of various colours was successfully demonstrated. The versatility of the method should allow it to be used for a variety of applications including real time metering of volumes in platforms, quantitative monitoring of a

design's performance in real time and the elimination of metering chambers in designs.

Abrégé

Les systèmes microfluidiques permettent la miniaturisation de techniques classiques d'analyse chimique en n'utilisant qu'une fraction du temps et des ressources requises conventionnellement. Ces systèmes offrent la possibilité d'effectuer des mesures directement sur le terrain sans avoir recours à un personnel qualifié. Des systèmes microfluidiques ont été développés qui utilisent la force centrifuge pour diriger le débit de liquides injectés et accomplir une variété de processus analytiques.

Bien que l'utilisation de la force centrifuge accorde à ces systèmes plusieurs avantages tels qu'un haut niveau de parallélisme, un potentiel de portabilité et la capacité de pomper des liquides indépendamment de leurs propriétés physicochimiques, elle crée aussi un modèle de conception qui requière l'accomplissement de toutes les opérations analytiques pendant que le système est en rotation.

En accord avec ce modèle, il est important de développer des techniques de mesure qui peuvent être appliquées pendant qu'un système microfluidique centrifuge est en mouvement. Une mesure importante est celle du volume de liquides injectés dans un système microfluidique centrifuge. La capacité d'effectuer la mesure des volumes directement sur des systèmes microfluidiques en mouvement pourrait permettre la quantification du débit de liquide en temps

réel et éliminer le besoin d'utiliser des chambres de comptage qui occupent un espace déjà restreint sur le système.

Dans cette thèse, une technique basée sur la segmentation d'images a été développée pour mesurer le volume d'aliquotes de liquide dans des systèmes microfluidiques en rotation. Des systèmes d'évaluation contenant une couche de peinture contrastante ont été conçus, fabriqués et injectés avec des aliquotes de liquides. Des images de haute résolution de ces systèmes en mouvement ont été acquises avec une caméra numérique à haute vitesse synchronisée avec une lumière stroboscopique et traitées numériquement. Ces images ont été converties à un espace colorimétrique de niveau de gris et segmentées pour tracer un contour autour de chaque aliquote de liquide. Ces contours ont ensuite été utilisés pour calculer l'aire de chaque aliquote qui a ensuite été divisée par l'aire d'une aliquote de calibration située sur la même image pour obtenir le volume de chaque aliquote.

La technique de mesure de volume a été caractérisée par des études conçus pour tester sa précision et son exactitude pour différents volumes. La précision et l'exactitude obtenues ont été de 1 et 2 % respectivement. Une caractérisation supplémentaire de la technique a révélé sa flexibilité quant au grandissement du système optique, la taille, la forme et le rapport hauteur/largeur des chambres du système et la fréquence de rotation du système. Une enquête sur les effets de la tension de surface du liquide mesuré sur la précision de la méthode a aussi été

effectuée. L'applicabilité de la technique à des liquides de diverses couleurs a aussi été démontrée avec succès. La versatilité de cette méthode devrait permettre son utilisation dans une variété d'applications incluant la mesure de volumes en temps réel, le contrôle quantitatif de la performance de designs de systèmes microfluidiques centrifuges en temps réel et l'élimination de chambres de comptage dans leur conception.

Acknowledgements

First and foremost, I would like to give my heartfelt thanks to my supervisor, Professor Eric D. Salin, for giving me the opportunity to be a part of his research group and introducing me to the world of centrifugal microfluidics. His humour, patience and wisdom guided me throughout my studies and his lab engineered a free-thinking, cultivating environment for my research.

My lab mates deserve my genuine appreciation for the helpful advice and friendly discussions over countless coffees, especially Erin Templeton, whose friendship warmed the office and whose dialogues inspired motivation during the tenure of my Masters studies. A colossal thanks to Dr. Matthew C. R. Kong, my mentor during my undergraduate honours project with the group, whose guidance encouraged independent thought and whose leadership enthused productivity. Thanks to Adam Bouchard and Laura Swayne for their insightful collaborations.

I would like to thank Dr. David Burns for stimulating discussions in chemometrics and a wide view of applications for analytical methods. Thanks to Timothy Mack for being my friend, colleague and undergraduate/ M. Sc. counterpart at McGill, and hopefully Ph.D. too!

Thanks to Dr. Sam Sewall and the undergraduate instrumental analysis laboratory staff for providing me with the opportunity to share my passion for analytical chemistry as a Teaching Assistant.

My unconditional thanks and love go out to my family, for their love and support throughout my education: Papa, Mama and Alice. Your unwavering belief in me inspired motivation to pursue my passions.

Last but certainly not least, I would like to give my utmost love and gratitude to Angelica Gopal, whose endless support rendered this thesis possible. Thank you for your patience and understanding, and your presence by my side during the long nights.

Table of Contents

List of Tables

List of Figures

List of Equations

1. Introduction

Modern chemical analysis relies on the use of specialized instrumentation to accurately quantify chemical species in many different domains. As the effectiveness of these instruments has continuously improved due to technical innovation, sample preparation has become the most time consuming step in analytical processes, sometimes taking up to 80% of an analyst's time[1]. Sample preparation often generates copious amounts of waste given the large amounts of solvents and reagents required in a typical process. This can cause a significant environmental hazard as well as increased operational costs for analytical laboratories. Furthermore, some samples must be shipped from distant sampling locations to laboratories, further driving up the cost of analysis and introducing the risk of sample contamination while in transit.

To meet these challenges, researchers have focused on the creation of portable miniaturized devices that can perform a variety of analytical operations while keeping analysis times and costs at a minimum[2]. The automation of analytical processes by micro-instrumentation offers a unique approach for chemical analysis that exchanges central lab based analyses for portable coin-sized integrated fluidic devices (Figure 1-1)[3] that are tailored for a specific analysis. These devices integrate all steps of an analytical process from sample preparation to results, utilize only microlitres of sample, solvents and reagents, perform

analyses within seconds and require little training for operators. While it is clear that laboratory based methods will remain the gold standard of chemical analysts, the continued development of portable miniaturized instrumentation offers a very interesting alternative for future developments.

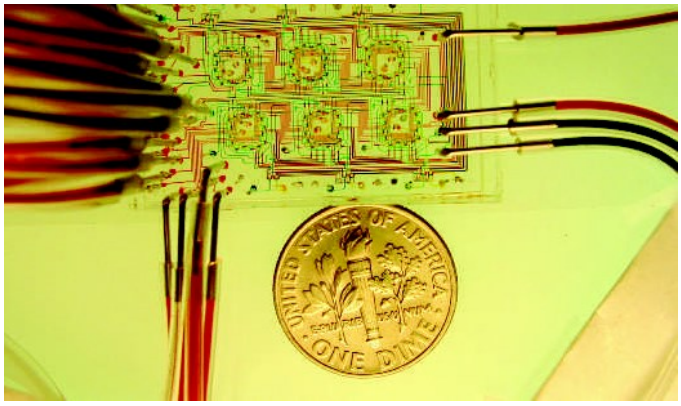

Figure 1-1: A microfluidic chemostat used to study the growth of microbial populations[3].

1.1 Microfluidics

1.1.1 Introduction to Microfluidics

Microfluidics, the science of manipulation of micro-amounts of fluids, is a critical component in the miniaturization of analytical instruments[3]. Combined with micro-electronics, microfluidics enables the construction of fully integrated analysis systems called micro total analysis systems (μ-TAS)[4] or "lab-on-a-chip" (LOC) devices that are capable of accomplishing all (or most) steps of an analytical process, such as sample preparation, separation, detection and readout on a single device.

The use of micro-volumes allows analyses performed on μ-TAS to minimize labour, time, cost and waste of reagents. Thanks to established methods in micro-engineering, the fabrication of microfluidic devices can be often be accomplished rapidly and inexpensively, leading to the possibility of cheap and disposable analytical tools[5].

Several comprehensive reviews of current microfluidic technologies illustrate the wide range of options available to microfluidic engineers and the variety of domains of application[6-10].

1.1.2 Microfluidic concepts

When scaled down to the microlitre level, fluids present interesting properties that must be taken into account for proper microfluidic engineering[11]. At the micro length scale of microfluidic devices, surface forces such as capillary action and viscosity are the dominant form of interaction. This opens the door to devices driven purely by capillary action, similar in concept to standard commercial pregnancy tests. In devices in which pumping is conducted by any other method, the dominance of surface properties introduces an important design limitation that must be considered.

In fluid mechanics, one aspect of liquid flow is characterized through the Reynolds number (Re), a dimensionless quantity that predicts if the liquid flow in a system is turbulent or laminar through the ratio of inertial forces to viscous forces.

$$Re = \frac{\rho v D_h}{\mu}$$

Equation 1-1: The Reynolds Number.

where ρ is the fluid density, v is the fluid velocity, $D_h$is the hydraulic diameter of a channel and μ is the fluid dynamic viscosity.

A low Re (<2000) indicates a laminar flow, a higher Re (>3000) denotes a turbulent flow while an Re in the transition region (2000-3000) shares characteristics of both flows[12]. Given the dimensions utilized in microfluidic devices, it is clear that the Reynolds number of such systems is typically very low, sometimes even below unity, assuring a completely laminar flow in most cases. Laminar flows have important consequences on mixing, which is then limited by molecular diffusion[13, 14]. For example, two laminar liquid streams that are brought together in a single channel will continue to flow in parallel with mixing only occurring at the common interface. While laminar flow allows for effective on-chip gradient generation[15-17], additional micromixing features are required if effective mixing is desired[18, 19].

1.1.3 Microfluidic platforms

Due to the considerable variety of design features and fabrication methods available to microfluidic engineers, it is important to establish guidelines to streamline the creation of lab-on-a-chip devices. Microfluidic designs are typically broken down into specialized modules called **unit operations** such as mixing,

metering, valving, transport, separation and detection. These unit operations are then (ideally) seamlessly integrated through a common interface using an established micro-fabrication technology to create a microfluidic platform which can then be used to create devices geared towards a particular application. Many different microfluidic platforms have been developed[6, 7] for analytical operations, each having its strengths and weaknesses in regards to specific applications.

The simplest and oldest microfluidic platform is the capillary driven lateral flow test, which uses capillary forces to drive a sample through a microfluidic system[20]. While they are fast, robust and inexpensive to fabricate and have a variety of applications in biomedical analysis, lateral flow tests are limited by the small number of possible consecutive operations and their reliance on capillary action, which restricts samples to those having certain surface properties.

Conventional microfluidics (*i.e.* non capillary flow driven) utilize mechanical elements to generate a pressure driven flow[13] that is used to move a sample inside a microfluidic chip. The driving pressure can be generated either off-chip through external pumps such as syringe pumps or on-chip pumping elements that are integrated directly into the device. These on-chip micro-pumps are typically composed of an embedded micro-diaphragm that is actuated pneumatically, thermally, magnetically or piezoeletrically and that can be combined in series with other diaphragms to create embedded peristaltic pumps[21]. The requirement for

external connections creates interfacing problems such as the introduction of air bubbles and poses limitations on the portability of some of these microfluidic devices. Integration of on-chip pumping resolves this issue while introducing additional challenges into the fabrication process, which needs to be adapted to accommodate the integrated components.

Droplet based or digital microfluidics (DMF)[22, 23] employs the electrowetting-on-dieletric (EWOD) effect for liquid pumping where an electric field is used to modify the contact angle of a conductive fluid in order to direct it within a microfluidic device. The injected liquid is sandwiched between two sets of electrodes which are insulated by a hydrophobic layer. The application of voltage between two neighbouring electrodes increases the wetting properties of the hydrophobic surface, actuating the droplet. Thanks to the programmability of the electrode network, DMF offers a very flexible operational platform that lends itself well for applications in biomedical analysis such as polymerase chain reaction assays[24] and DNA sequencing[25] as well as in sample preparation for mass spectrometry[26] and other analytical detection methods[27]. Despite this flexibility, DMF devices require expensive control instrumentation, do not yet show potential for portability and are overall better suited for sample preparation for bench top instruments. In addition, the use of the EWOD effect for pumping introduces the risk of electrolysis of samples and requires conductive samples.

Electrokinetic platforms present another non-mechanical approach to microfluidic design. These platforms exploit several electrokinetic effects for flow control such as electro-osmosis[28, 29] to transport liquids inside the device without the use of moving parts and electrophoresis[30, 31] to separate charged analytes. The innate capability of separations by electrophoresis renders this platform attractive for biochemical applications that conventionally utilize capillary electrophoresis for analysis of biological molecules. Similarly to digital microfluidics, the use of micro-electrodes in electrokinetic devices allows for very precise control over metering of samples. Although the electrokinetic microfluidic platform delivers a robust package for many applications, its usage in the conception of μ-TAS is limited. Generation of the high voltage electric field essential for platform operation makes the development of portable devices very difficult. In addition, the requirement for sample conductivity restricts the use of this platform to a limited number of analytes.

An important alternative solution to microfluidic design is the centrifugal microfluidic (CM) platform[32], which utilizes centrifugal force to direct liquids inside the device. As this was the chosen platform for the experiments in this thesis, a detailed description follows in the next subsection.

1.2 Centrifugal Microfluidics : A Detailed Platform Description

1.2.1 Platform Overview

Since the development of the first computer interfaced fast centrifugal analyzers in 1969[33], research into centrifugal microfluidic platforms has experienced significant growth owing to their potential for the development of complete μ-TAS, resulting in complete commercial systems such as the LabCD™ by Tecan[34], the Picollo™ by Abaxis[35] and the Gyros MALDI™ by Gyros AB[36]. These platforms, also known as Lab-on-a-CD[37] due to their shape generally resembling a compact disc, offer the ability to perform many analytical unit operations by using centrifugal force for flow actuation and control.

The use of centrifugal force to drive microfluidic systems provides many direct advantages. Pumping by centrifugal force is not influenced by the physicochemical properties of the pumped liquid with the exception of viscosity[37]. This allows the use of any liquid inside a CM platform providing that it is tolerated by the chemistry of the substrate used in the platform's fabrication. Operation of CM platforms only requires a small motor and can easily be made portable for in-field use[38]. Valving[39] can be readily accomplished through use of hydrophobic or capillary based valves that require a minimum level of centrifugal pressure to open. This allows easy flow control through variations in rotational frequency. As centrifugal force is uniform at any given radial position, CM platforms demonstrate a native capability for

parallel analyses accomplished in identical structures under similar conditions, as exemplified by the 104 parallel immunoassay cells of the Gyrolab Bioaffy^{tm} device produced by Gyros[40].

The theoretical background and physics behind centrifugal microfluidics has been described in detail in several review articles[37, 41-43]. Applications of CM platforms to many chemical and biochemical analysis methodologies have been demonstrated, such as sample preparation by liquid-liquid extraction[44], colorimetric analysis of glucose levels in blood[45], polymerase chain reaction (PCR) DNA amplification[46], enzyme-linked immunosorbent assays (ELISA)[47] and DNA Microarrays[48]. Other applications abound in environmental chemical analysis where CM platforms have been utilized to analyze levels of nutrients in water[49], spent nuclear fuels[50], nitrates and nitrites[51], sulfides[52] and polycyclic aromatic hydrocarbons (PAHs)[53].

1.2.2 Platform limitations

While centrifugal microfluidic platforms offers considerable potential for miniaturized chemical analysis, they face an important constraint that limits their usability for complex operations. Since centrifugal force is unidirectional, it restricts the amount of useable platform space to the radius of the platform. This issue, sometimes called the “real estate” problem[54], limits the number of consecutive unit operations that can be included on a single platform. While several methods of

active pumping have been developed to attempt to overcome this drawback[55-58], it is valuable to engineer features that utilize the least amount of real estate while providing the desired functionality to compensate for this challenge.

Centrifugal force provides a powerful method of flow control on CM platforms. While a CM platform is in motion, the force can keep the liquid flowing along a known path down the radius of the device. If the liquid reaches a valve that it is unable to breach due to insufficient force, centrifugal force keeps the liquid contained in the chamber located directly above the valve. However, this type of flow control enforces an important paradigm on the design of CM platforms that requires that all unit operations be performed while the platform is in motion. Stopping the platform may result in unintended capillary induced flow in channels that could cause both a loss of sample and a disruption of the intended mode of operation[56]. While most fluidic operations require that a CM platform be in motion, measurement and detection methods must be adapted to accommodate this paradigm.

1.3 Volume Measurements on Centrifugal Microfluidic Platforms in Motion

1.3.1 Volume Metering Chambers

Analytical methodology requires the accurate knowledge of sample and reagent volumes to deliver accurate determinations. On CM platforms, this condition is normally met through metering of both samples and reagents via the

use of metering chambers[37]. Typically, metering chambers dispense a fixed amount of liquid based on the physical dimensions of the chamber, with all remaining liquid past the metered level going to a waste overflow channel as can be seen on Figure 1-2[41].

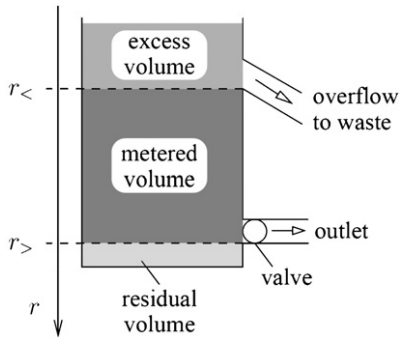

Figure 1-2: Example of a standard metering chamber utilized on CM designs. The chamber is first filled by spinning the platform at a frequency insufficient to burst the valve at the bottom of the chamber and with all excess volume going to waste. The metered volume is then released to the next unit operation through an increase in rotational frequency.

While metering chambers are a valuable feature in the CM toolbox, they suffer from two disadvantages. First, they occupy valuable real estate on the platform, especially if metering of several reagents is required. Second, they can only meter out a specific volume, rendering them inflexible. These factors encourage the development of alternate volume measurement methods that meet the precision needs of analytical methodology.

1.3.2 Real Time Volume Measurements

1.3.2.1 Ideal Criteria for Multipurpose Volume Measurements

To overcome the need for metering chambers on CM platforms, novel volume measurement techniques must be developed. The capability to measure volumes directly on CM platforms in motion could not only allow experimenters to avoid the use of metering chambers but also to quantify liquid flow in real time. This would allow evaluation of the performance of CM platforms while in motion. As indicated in section 1.2.2, this is of high importance since CM platforms are designed to be constantly subjected to centrifugal force during operation.

An ideal volume measurement technique for CM platforms should be contactless to facilitate measurements in motion, limit the introduction of additional design features due to real estate limitations and avoid the use of specialized equipment so it can be adapted to fit any experimental setup. Since chambers and features on CM platforms come in a variety of shapes, the technique should utilize the least amount of prior knowledge about the device design and the properties of the liquid to be measured. Finally, the measurement process should be as automated as possible to limit the introduction of operator error.

While application-specific volume measurements on microfluidic platforms have been successfully accomplished through methods such as the use of impedance measurements on an EWOD platform[59], total internal reflection of a

laser beam on a single channel in a CM platform[60], or microscopy images of water-in-oil droplets[61], there is currently a lack of a robust, multipurpose volume measurement technique for CM platforms in motion.

1.3.2.2 Optical Solutions

Optical methodologies provide an approach that is well suited to the challenges presented by volume measurements on CM platforms due to their ability to provide near-instantaneous non-contact measurements that can be electronically synchronized with platform rotation. An example of such a method is the use of the total internal reflection of a laser beam along a single channel to obtain real time volume measurements for liquids flowing through the channel[60]. While this method provides adequate precision figures for the determined volumes, it is limited to measurements along a single channel, requires the difficult micro-machining of channels having a triangular cross section on both sides of the measurement channel and relies on additional specialized electronics to synchronize the measurement.

Optical imaging is commonly used to visually and qualitatively monitor the performance of CM platforms through real time images acquired with a high speed camera and strobe system that is synchronized with the platform position[62]. Further information can be extracted from these images by image analysis to provide dimensional measurements. To verify the volume of metered fluids, a

method has been described that uses manual processing of platform images acquired by a stroboscopic high speed camera to obtain a pixel count that is converted to a volume through a substrate based reference scale[63]. Although the use of image-based measurements provides a solid foundation, the requirements for a coloured liquid, manual image processing, a specialized stroboscopic microscope setup[64] and the integration of a substrate-based reference for every design feature on the platform renders this method too specific to be used for general purpose volume measurements on CM platforms. Further investigation of image analysis based methodologies is necessary if a method fulfilling the criteria outlined in section 1.3.2.1 is to be developed.

1.4 Enabling Real Time Volume Measurements by Image Processing

1.4.1 Basics of Digital Image Processing

Digital image processing is a potent computational tool that has been used in a variety of microfluidic domains to perform dimensional measurements, including the areas, volumes and deformability of erythrocytes injected into a microfluidic device[65, 66], the haematocrit of blood on a diagnostics platform[67] and the volume of generated droplets on an EWOD device[68].

Basic image processing operations can be broken down into two main categories: **image enhancement,** which provides tools to improve specific features of an image, and **image analysis,** which can be used to obtain information from

images. The main processes utilized for the development of the volume measurement technique described in this thesis can be found in the next subsections.

1.4.1.1 Images: Definition, Acquisition and Storage

A digital image consists of a two dimensional array of picture elements (pixels) that store a spatially distributed intensity signal *f(x,y)* where *f* is the intensity of the pixel and *x* and *y* are a set of coordinates that locate the pixel along a pair of orthogonal axes[69]. The intensity level of each pixel is quantized to a finite level during the acquisition of the image from a real continuous signal by a digital camera, with the number of available levels being determined by the resolution of the camera.

A coloured image can be defined as an extension of a standard image *f(x,y)* with the addition of a color channel parameter to store the colour information. This can be generalized into a colour image *g(x,y,c)* where *g* is the intensity for a pixel located at the *x* and *y* coordinates for the color channel *c* which is either red (R), green (G) or blue (B) due to the widespread use of the RGB colour model[70].

Most image processing operations are designed to utilize only a single intensity plane. In the case of colour images, this requires either the isolation of a single colour channel or the extraction of intensity information (luminance) from all colour channels to obtain a single intensity value per pixel. The latter process is called

grayscale conversion[71] since the resulting images are often displayed as shades of gray, starting from black for an intensity of 0 and progressing towards white, which represents that largest intensity level. A typical grayscale conversion algorithm retains the overall luminance of the image by utilizing a weighted sum of the colour channel intensities to account for the non-linear perception of colour[71].

$$f(x,y) = 0.299 \times\ g(x,y,R) + 0.587\ \times\ g(x,y,G) + 0.114 \times g(x,y,B)$$

Equation 1-2: Grayscale conversion using standard coefficients defined by the National Television Systems Committee (NTSC)

1.4.1.2 Digital Image Filtering

A key component of many digital image processing operations is the use of local operators called filters. Filtering of an image involves the convolution of a coefficient array called a kernel on every pixel of the image[69]. A kernel can be defined as an array *w(i,j)* with a size *of 2I+1* by *2J+1* pixels and centered around *(i,j)* = (0,0).

$$h(x,y) = w(i,j) * f(x,y) = \sum_{i=-I}^{I} \sum_{j=-J}^{j} w(i,j) \times f(x-i, y-j)$$

Equation 1-3: Convolution of a digital filter kernel on an image f(x,y)

where *h(x,y)* is the result of the convolution of the *w(i,j)* kernel on a pixel of the *f(x,y)* image. In simple terms, this convolution involves the alignment of the kernel on top of the pixel of choice so that *(i,j)* = (0,0) at the position of *(x,y)* followed by

the cross multiplication of each kernel coefficient with the corresponding image pixel. This process is then repeated for every pixel of *f(x,y)* to obtain the filtered image *h(x,y).* Pixels located at the edge of the image are ignored as parts of the kernel would extend beyond the image boundaries. Further mentions of digital image filtering refer to the use of this operation with various kernels.

1.4.2 Image Enhancement

Real images present several traits that can impact their utility for analytical applications. Similarly to most signals obtained from digital instruments, images present a susceptibility to noise. Imaging of objects in motion such as CM s platforms introduces an unwanted blurring effect, which reduces the edge contrast of the obtained image. Well defined edges are not only important for visualization but also for certain image analysis techniques such as segmentation. Images can also potentially suffer from poor contrast depending on the lighting system and background that are utilized during the acquisition process. To remedy these factors, several simple image enhancement methods are available.

Noise reduction is commonly accomplished through the use of mean, Gaussian filters or median filters.[72] A mean filter, such as the one used in Figure 1-3B, uses a kernel that calculates the mean of all pixels located in its range and returns this value to the pixel on which the kernel is centered. While effective at reducing noise similarly to the use of a moving average on one dimensional

signals, this method has a significant negative impact on edge contrast. To reduce the blurring of edges, one solution is to weight the contribution of neighboring pixels according to their distance from the center of the kernel by the use of a two dimensional Gaussian function to create a Gaussian filter *gf(i,j)*

$$gf(i,j) = \frac{1}{2\pi\sigma^2} e^{-\frac{i^2+j^2}{2\sigma^2}}$$

Equation 1-4: Computation of a Gaussian filter

where *i* is the distance from kernel origin in the horizontal axis, *j* is the distance from kernel origin in the vertical axis and σ is the standard deviation of the Gaussian function. An example of such a filter can be found on Figure 1-3C.

Median filtering is a non-linear alternative that computes the median of each pixel's neighborhood. A key property of median filtering is that it is capable of preserving edges while removing small amplitude noise[73]. A demonstration of this filter can be found on Figure 1-3D.

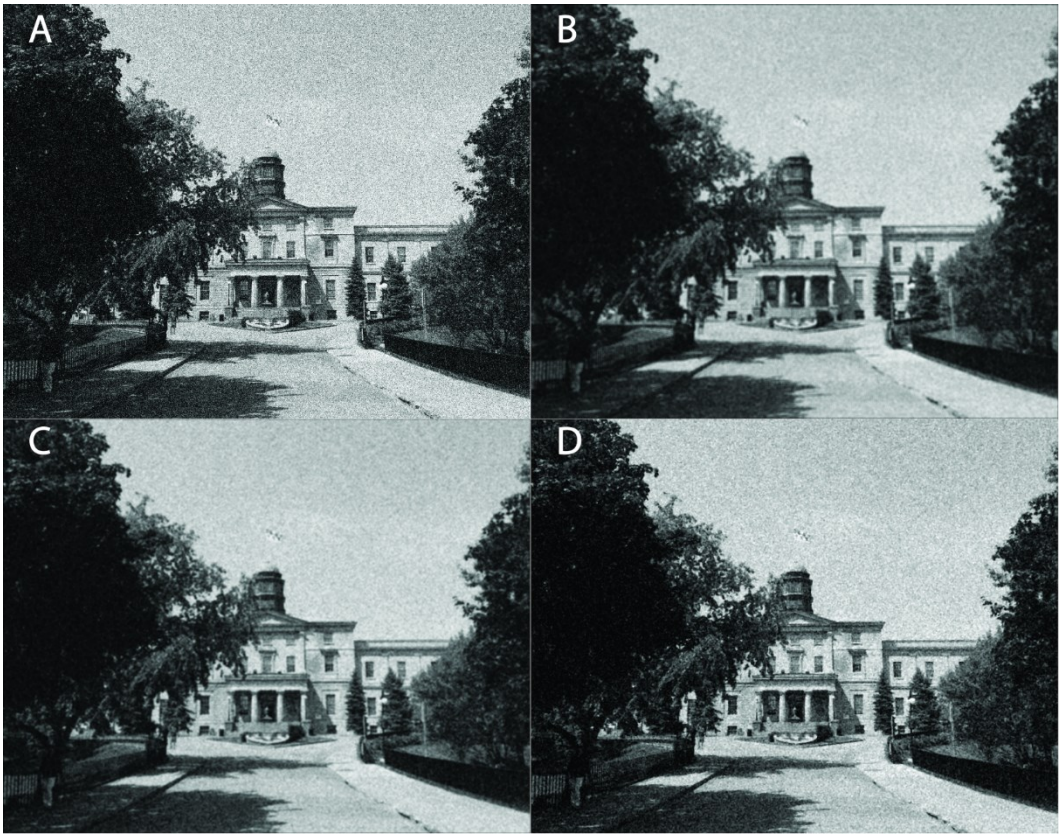

Figure 1-3: Demonstration of noise reduction techniques. A) Grayscale image corrupted by the addition of Gaussian noise. B) 5 by 5 mean filter applied to image A. C) 5 by 5 Gaussian filter with a σ of 1.5 applied to image A. D) 5 by 5 median filter applied to image A.

Poorly resolved edges can be improved through unsharp masking[69, 72]. This technique first applies a Gaussian filter to the image before subtracting the blurred version from the original image to obtain a sharpened image. This effect occurs because the edges of an image in frequency space are mainly composed of high frequency components as they are abrupt transitions in intensity. Since a Gaussian filter blurs the image, it is effectively a low-pass filter that reduces the high frequency content of the image. The subtraction of the blurred image from the original results in a high-pass filter: the high frequency components of the image's

edges are emphasized by the reduction in low-frequency components. A demonstration of unsharp masking can be found on Figure 1-4B.

Inadequate image contrast due to glare or poor lighting can often be efficiently resolved through intensity scaling[69]. This process increases the linear dynamic range of the image by stretching a specific intensity range (R_{min} to R_{max}) over the maximum number of intensity levels. This range is chosen by saturating a select percentage of image pixels at both low and high intensities based on the cumulative distribution function of the image histogram. Any pixels whose intensity lies below this range is assigned the intensity level of 0, whereas any pixel above this range is brought to the highest possible intensity level. All pixels intensities in between are then normalized to span the full range of the image.

$$f_{adj}(x,y) = \frac{f(x,y) - R_{min}}{R_{max} - R_{min}} \times f_{max}$$

Equation 1-5: Intensity scaling of an image

Where $f_{adj}(x,y)$ is the scaled image, $f(x,y)$ is the original image, R_{min} is the bottom of the chosen range, R_{max} is the top of the chosen range and f_{max} is the maximum intensity level of the image. An example of intensity scaling can be found on Figure 1-4C.

Figure 1-4: Demonstration of contrast enhancement and sharpening techniques. A) Original grayscale image. B) 3 by 3 unsharp filter applied to image A. C) Intensity scaling applied to image A by saturating top and bottom 1% of pixels.

1.4.3 Image Analysis by Segmentation

Dimensional analysis can be readily accomplished on images by the use of a process called image segmentation[74]. Image segmentation involves the partitioning of an image into distinct regions sharing common characteristics. By applying segmentation to an image, features of interest can be identified for automatic measurement.

A variety of image segmentation techniques are available[74-76], the choice of which depends on the required application. Typically, segmentation techniques

can be separated into two main categories: **region- based** segmentation, which separates regions in an image based on common criteria, and **edge-based segmentation,** which directly detects the edges that separate regions.

1.4.3.1 Region-Based Segmentation

Region-based segmentation includes global thresholding, region growing and the watershed algorithm[77]. Global thresholding involves the partition of the image into two classes, the background and the foreground through the selection of a threshold intensity level. All pixels whose intensity is equal to or lower than the threshold are classed as the background while pixels whose intensity is higher than the threshold are classed as the foreground. Selection of an appropriate threshold can be made automatic through a method developed by Otsu that minimizes intra-class variance[78]. Such a method is only useful for ideal images where only two components are clearly visible.

Region growing utilises a seed point to find a region of pixels that share similar intensities through iteration. Following selection of a seed point, the neighboring pixels are examined and added to the region if their intensity meets a uniformity criterion such as the mean of the existing region. The effectiveness of this technique relies on the proper choice of a seed point and uniformity criterion and relatively noiseless images.

The watershed algorithm[79] uses a topographic approach to identify regions through seeded markers. The different intensity levels of the image can be conceptually seen as the altitude in a topographic relief. Pixels of high intensities represent peaks while pixels of low intensities denote valleys. To begin segmentation, seed markers are chosen in areas of interest. The relief is then "flooded" from these markers and the "water" level begins to rise. However, the water basin originating from each marker is not allowed to mix so "dams" must be drawn to isolate them. These dams represent the edges of each region. Proper utilization of the watershed algorithm requires very careful selection of markers as the alternative often leads to over-segmentation that is exacerbated by noise.

1.4.3.2 Edge—Based Segmentation

Edge-based segmentation techniques identify boundaries between different regions of an image and are primarily derivative-based. One significant advantage to edge-based segmentation is that it does not require any prior knowledge about the image contents. However, the derivative-based methodology renders this type of segmentation vulnerable to the localization of false edges due to noise. The most common edge-based techniques are the Canny[80, 81] method and the Hildreth-Marr or Laplacian-of-Gaussian (LoG) operator[82, 83].

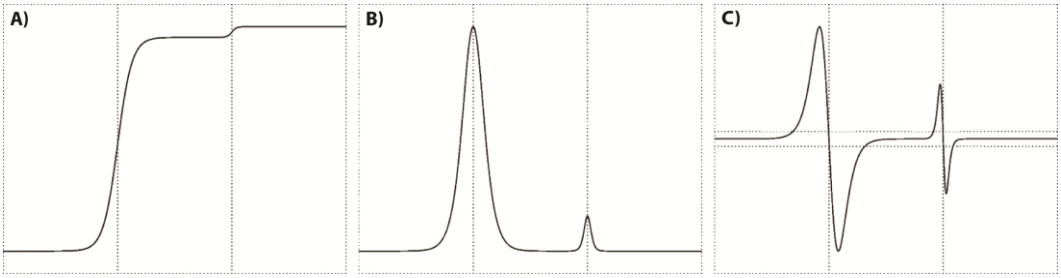

Figure 1-5: A one dimensional example of typical edge detection strategies. A) A one dimensional signal that includes two edges. B) The first derivative of the signal C) The second derivative of the signal.

An edge in an image is typically defined as a sharp variation in intensity (Figure 1-5A)[77]. An initial strategy for edge detection is the computation of the intensity gradient (Figure 1-5B), which is an approximation of the first derivative of the image intensity.

$$G(x,y) = \sqrt{\left(\frac{\partial f}{\partial x}\right)^2 + \left(\frac{\partial f}{\partial y}\right)^2} = \sqrt{G_x^2 + G_y^2}$$

Equation 1-6: Computation of the image gradient magnitude

Where *G(x,y)* is the gradient magnitude, *f(x,y)* is the image intensity, G_x and G_y are the gradients in the *x* and *y* direction. Since image intensities are discrete in nature, they must be differentiated through a discrete difference operator. This is most commonly done through the Sobel operator that uses two difference filters to obtain gradients in both orientations.

$$G_x = \begin{bmatrix} -1 & -2 & -1 \\ 0 & 0 & 0 \\ 1 & 2 & 1 \end{bmatrix} \qquad G_y = \begin{bmatrix} -1 & 0 & 1 \\ -2 & 0 & 2 \\ -1 & 0 & 1 \end{bmatrix}$$

Equation 1-7: Kernels used to calculate intensity gradients in the x and y orientations

As can be seen on Figure 6B, the maximum of the gradient should correspond to the exact location of the edge. However, this criterion is insufficient when dealing with real images, where the transition in intensity at the edge is smoother, noisier and less obvious. The gradient of such an edge presents a much wider spread that renders the exact spatial localization difficult. To deal with such cases, a more advanced methodology is required, the most common being the Canny[81] method of segmentation.

The Canny method begins by the Gaussian filtering of the image to reduce false edges due to noise. The gradient of the image intensity is then calculated via the Sobel operator after which the gradient angle θ for each pixel is computed trigonometrically from its gradients in the x and y directions:

$$\theta = \arctan\left(\frac{G_y}{G_x}\right)$$

Equation 1-8: Calculation of the gradient angle

To find a single location for each real edge, an algorithm of non-maximum suppression is applied to all pixels. The gradient angle θ of all pixels is first rounded to the closest multiple of 45 degrees to determine the potential edge direction, which is always perpendicular to the rounded gradient angle. The gradient magnitude of the potential edge pixel is then compared to the two immediate neighbors lying in the same edge direction and an edge is declared only if this gradient magnitude is larger than that of the two neighbors. The edge detection

process is finalized by thresholding all edge-flagged pixels by hysteresis to ensure that only genuine edges are returned. First, an upper gradient magnitude threshold is selected above which all edges are declared as strong. A second, lower threshold is used to declare weak edges if they originate from a strong edge. The result of the segmentation is a binary image in which edge points are marked as 1s while all other pixels are marked as 0s. An example of a Canny segmented image can be found on Figure 1-6B.

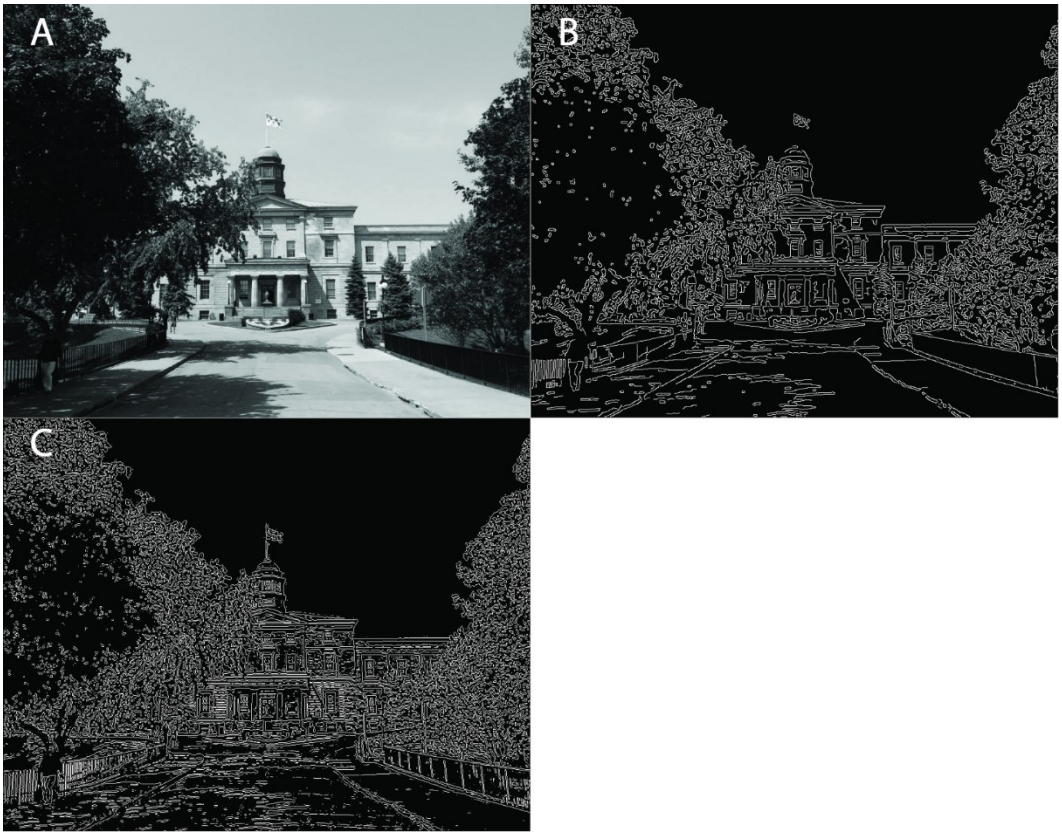

Figure 1-6: Example of edge-based segmentation techniques. A) Original grayscale image. B) Canny method applied to A with a Gaussian σ of 1.5. C) Laplacian of Gaussian method applied to A with a Gaussian σ of 1.5.

An alternative approach to image segmentation utilizes the second derivative of the image intensity which is also known as the divergence of the gradient. As can be seen in Figure 1-5C, the second derivative of an edge presents a zero at the exact location of an edge. This enables the easy detection of edges through the search for zero crossings in the second derivative of the data. A powerful method that utilizes this approach is the Marr-Hildreth or Laplacian-of-Gaussian(LoG)[83] operator. This method begins by the application of a Gaussian filter to the target image as the differentiation process is particularly sensitive to noise. The second derivative *L(x,y)* of the image *f(x,y)* can be calculated through application of a Laplacian operator.

$$L(x,y) = \nabla^2 f(x,y) = \sqrt{\left(\frac{\partial^2 f}{\partial x^2}\right)^2 + \left(\frac{\partial^2 f}{\partial y^2}\right)^2}$$

Equation 1-9: Computation of the second derivative or divergence of gradient of an image

Before application to the image, the Laplacian operator can be convolved directly on the Gaussian filter gf(i,j), yielding a Laplacian-of-Gaussian filter:

$$LoG(i,j) = \nabla^2 * gf(i,j) = -\frac{1}{\pi\sigma^4}\left[1 - \frac{i^2+j^2}{2\sigma^2}\right] e^{\frac{-i^2+j^2}{2\sigma^2}}$$

Equation 1-10: Laplacian of Gaussian Filter

A discrete approximation of this filter is then applied to the image to compute its divergence of the intensity.

$$LoG = \begin{bmatrix} -0.4 & -0.8 & -0.4 \\ -0.8 & 4.8 & -0.8 \\ -0.4 & -0.8 & -0.4 \end{bmatrix}$$

Equation 1-11: Laplacian of Gaussian Kernel with a σ of 0.5

The obtained derivative is then scanned for zero-crossings to identify edges. In practice, because of the discrete nature of images, it is possible for a real zero crossing not to exist. In this case, the closest value to zero must be used instead. The resulting edges are then thresholded to ensure that only genuine edges are detected. An application of the LoG method to the segmentation of an image can be found on Figure 1-6C.

1.5 Thesis objective

The objective of this thesis is to develop and characterize a technique to measure volumes of liquid aliquots inside CM platforms in-motion through an approach based on the automatic image segmentation of platform images. Direct volume measurements offer the potential for the development of CM analytical methods that require precise volume knowledge without the need for metering chambers, saving valuable real estate on CM platforms. The ability to measure volumes in real time will also allow quantitative evaluation of platform designs, a task that has previously been difficult to accomplish due to the challenge presented by in-motion measurements. The demonstrated technique is versatile, flexible

towards the needs of experimenters and does not require any additional components beyond those included on a typical CM experimental apparatus.

1.6 Thesis outline

Chapter 2 describes the CM platforms used to investigate the volume measurement technique as well as the imaging instrumentation and experimental apparatus utilized for synchronized acquisition of images of platforms in motion.

Chapter 3 introduces the volume measurement algorithm and offers a figure of merit characterization of the method on ideal and real platforms using pre-metered aliquots.

Chapter 4 presents an extended evaluation of method performance based on several experimental parameters, such as optical magnification, platform rotational frequency, design feature shape, liquid surface properties and liquid color.

Chapter 5 summarizes the conclusions of the research and discusses potential applications and future directions for the developed volume measurement technique.

1.7 References

1. Y. Chen, Z. Guo, X. Wang and C. Qiu,"Sample preparation", *Journal of chromatography. A*, **2008**, 1184, 191-219.

2. A. Rios, M. Zougagh and M. Avila,"Miniaturization through lab-on-a-chip: Utopia or reality for routine laboratories? A review", *Anal Chim Acta*, **2012**, 740, 1-11.

3. G. M. Whitesides,"The origins and the future of microfluidics", *Nature*, **2006**, 442, 368-373.

4. D. R. Reyes, D. Iossifidis, P.-A. Auroux and A. Manz,"Micro Total Analysis Systems. 1. Introduction, Theory, and Technology", *Analytical chemistry*, **2002**, 74, 2623-2636.

5. H. Kido, J. Zoval and M. J. J. Madou,"Rapid Prototyping of Microfludic Systems", **2007**, 4, 101-105.

6. S. Haeberle and R. Zengerle,"Microfluidic platforms for lab-on-a-chip applications", *Lab on a chip*, **2007**, 7, 1094-1110.

7. D. Mark, S. Haeberle, G. Roth, F. von Stetten and R. Zengerle,"Microfluidic lab-on-a-chip platforms: requirements, characteristics and applications", *Chemical Society reviews*, **2010**, 39, 1153-1182.

8. P. N. Nge, C. I. Rogers and A. T. Woolley,"Advances in Microfluidic Materials, Functions, Integration, and Applications", *Chemical reviews*, **2013**, DOI: 10.1021/cr300337x.

9. M. L. Kovarik, D. M. Ornoff, A. T. Melvin, N. C. Dobes, Y. Wang, A. J. Dickinson, P. C. Gach, P. K. Shah and N. L. Allbritton,"Micro total analysis systems: fundamental advances and applications in the laboratory, clinic, and field", *Analytical chemistry*, **2013**, 85, 451-472.

10. J. West, M. Becker, S. Tombrink and A. Manz,"Micro total analysis systems: latest achievements", *Analytical chemistry*, **2008**, 80, 4403-4419.

11. H. A. Stone and S. Kim,"Microfluidics: Basic issues, applications, and challenges", *AIChE Journal*, **2001**, 47, 1250-1254.

12. T. Squires and S. Quake,"Microfluidics: Fluid physics at the nanoliter scale", *Reviews of Modern Physics*, **2005**, 77, 977-1026.

13. H. A. Stone, A. D. Stroock and A. Ajdari,"Engineering Flows in Small Devices", *Annual Review of Fluid Mechanics*, **2004**, 36, 381-411.

14. A. E. Kamholz and P. Yager,"Theoretical Analysis of Molecular Diffusion in Pressure-Driven Laminar Flow in Microfluidic Channels", *Biophysical journal*, **2001**, 80, 155-160.

15. N. L. Jeon, S. K. W. Dertinger, D. T. Chiu, I. S. Choi, A. D. Stroock and G. M. Whitesides,"Generation of Solution and Surface Gradients Using Microfluidic Systems", *Langmuir*, **2000**, 16, 8311-8316.

16. J. Pihl, J. Sinclair, E. Sahlin, M. Karlsson, F. Petterson, J. Olofsson and O. Orwar,"Microfluidic gradient-generating device for pharmacological profiling", *Analytical chemistry*, **2005**, 77, 3897-3903.

17. D. Irimia, D. A. Geba and M. Toner,"Universal microfluidic gradient generator", *Analytical chemistry*, **2006**, 78, 3472-3477.

18. L. E. Locascio,"Microfluidic mixing", *Analytical and bioanalytical chemistry*, **2004**, 379, 325-327.

19. C. Y. Lee, C. L. Chang, Y. N. Wang and L. M. Fu,"Microfluidic mixing: a review", *International journal of molecular sciences*, **2011**, 12, 3263-3287.

20. G. A. Posthuma-Trumpie, J. Korf and A. Amerongen,"Lateral flow (immuno)assay: its strengths, weaknesses, opportunities and threats. A literature survey", *Analytical and bioanalytical chemistry*, **2008**, 393, 569-582.

21. B. D. Iverson and S. V. Garimella,"Recent advances in microscale pumping technologies: a review and evaluation", *Microfluidics and Nanofluidics*, **2008**, 5, 145-174.

22. M. G. Pollack, A. D. Shenderov and R. B. Fair,"Electrowetting-based actuation of droplets for integrated microfluidics", *Lab on a chip*, **2002**, 2, 96-101.

23. C. Sung Kwon, M. Hyejin and K. Chang-Jin,"Creating, transporting, cutting, and merging liquid droplets by electrowetting-based actuation for digital microfluidic circuits", *Journal of Microelectromechanical Systems*, **2003**, 12, 70-80.

24. Y. H. Chang, G. B. Lee, F. C. Huang, Y. Y. Chen and J. L. Lin,"Integrated polymerase chain reaction chips utilizing digital microfluidics", *Biomed Microdevices*, **2006**, 8, 215-225.

25. R. B. Fair,"Digital microfluidics: is a true lab-on-a-chip possible?", *Microfluidics and Nanofluidics*, **2007**, 3, 245-281.

26. A. E. Kirby and A. R. Wheeler,"Digital microfluidics: an emerging sample preparation platform for mass spectrometry", *Analytical chemistry*, **2013**, 85, 6178-6184.

27. Y. Zhu and Q. Fang,"Analytical detection techniques for droplet microfluidics--a review", *Anal Chim Acta*, **2013**, 787, 24-35.

28. S. Arulanandam and D. Li,"Liquid transport in rectangular microchannels by electroosmotic pumping", *Colloids and Surfaces A: Physicochemical and Engineering Aspects*, **2000**, 161, 89-102.

29. X. Wang, C. Cheng, S. Wang and S. Liu,"Electroosmotic pumps and their applications in microfluidic systems", *Microfluid Nanofluidics*, **2009**, 6, 145.

30. Z. L. Fang and Q. Fang,"Development of a low-cost microfluidic capillary-electrophoresis system coupled with flow-injection and sequential-injection sample introduction (review)", *Fresenius' Journal of Analytical Chemistry*, **2001**, 370, 978-983.

31. J. Rossier, F. Reymond and P. E. Michel,"Polymer microfluidic chips for electrochemical and biochemical analyses", *Electrophoresis*, **2002**, 23, 858-867.

32. J. Ducrée, in *Encyclopedia of Microfluidics and Nanofluidics*, ed. D. Li, Springer US, 2008, DOI: 10.1007/978-0-387-48998-8_203, ch. 203, pp. 234-245.

33. N. G. Anderson,"Computer interfaced fast analyzers", *Science*, **1969**, 166, 317-324.

34. G. E. Cohn, M. J. Madou and G. J. Kellogg,"<title>LabCD: a centrifuge-based microfluidic platform for diagnostics</title>", **1998**, 3259, 80-93.

35. C. T. Schembri, T. L. Burd, A. R. Kopfsill, L. R. Shea and B. Braynin,"Centrifugation and Capillarity Integrated into a Multiple Analyte Whole-Blood Analyzer", *J Autom Chem*, **1995**, 17, 99-104.

36. R. Ehrnstrom,"Miniaturization and integration: challenges and breakthroughs in microfluidics", *Lab on a chip*, **2002**, 2, 26N-30N.

37. M. Madou, J. Zoval, G. Jia, H. Kido, J. Kim and N. Kim,"Lab on a CD", *Annual review of biomedical engineering*, **2006**, 8, 601-628.

38. M. Czugala, D. Maher, F. Collins, R. Burger, F. Hopfgartner, Y. Yang, J. Zhaou, J. Ducrée, A. Smeaton, K. J. Fraser, F. Benito-Lopez and D. Diamond,"CMAS: fully integrated portable centrifugal microfluidic analysis system for on-site colorimetric analysis", *RSC Advances*, **2013**, 3, 15928.

39. A. LaCroix-Fralish, E. J. Templeton, E. D. Salin and C. D. Skinner,"A rapid prototyping technique for valves and filters in centrifugal microfluidic devices", *Lab on a chip*, **2009**, 9, 3151-3154.

40. N. Honda, U. Lindberg, P. Andersson, S. Hoffmann and H. Takei,"Simultaneous multiple immunoassays in a compact disc-shaped microfluidic device based on centrifugal force", *Clinical chemistry*, **2005**, 51, 1955-1961.

41. J. Ducree, S. Haeberle, S. Lutz, S. Pausch, F. von Stetten and R. Zengerle,"The centrifugal microfluidic bio-disk platform", *J Micromech Microeng*, **2007**, 17, S103-S115.

42. T. H. Thio, S. Soroori, F. Ibrahim, W. Al-Faqheri, N. Soin, L. Kulinsky and M. Madou,"Theoretical development and critical analysis of burst frequency equations for passive valves on centrifugal microfluidic platforms", *Medical & biological engineering & computing*, **2013**, 51, 525-535.

43. R. Gorkin, J. Park, J. Siegrist, M. Amasia, B. S. Lee, J. M. Park, J. Kim, H. Kim, M. Madou and Y. K. Cho,"Centrifugal microfluidics for biomedical applications", *Lab on a chip*, **2010**, 10, 1758-1773.

44. A. Kazarine, M. C. Kong, E. J. Templeton and E. D. Salin,"Automated liquid-liquid extraction by pneumatic recirculation on a centrifugal microfluidic platform", *Analytical chemistry*, **2012**, 84, 6939-6943.

45. J. Steigert, M. Grumann, T. Brenner, K. Mittenbuhler, T. Nann, J. Ruhe, I. Moser, S. Haeberle, L. Riegger and J. Riegler,"Integrated Sample Preparation, Reaction, and Detection on a High-frequency Centrifugal Microfluidic Platform", *Journal of the Association for Laboratory Automation*, **2005**, 10, 331-341.

46. M. Focke, F. Stumpf, B. Faltin, P. Reith, D. Bamarni, S. Wadle, C. Muller, H. Reinecke, J. Schrenzel, P. Francois, D. Mark, G. Roth, R. Zengerle and F. von Stetten,"Microstructuring of polymer films for sensitive genotyping by real-time PCR on a centrifugal microfluidic platform", *Lab on a chip*, **2010**, 10, 2519-2526.

47. S. Lai, S. Wang, J. Luo, L. J. Lee, S. T. Yang and M. J. Madou,"Design of a compact disk-like microfluidic platform for enzyme-linked immunosorbent assay", *Analytical chemistry*, **2004**, 76, 1832-1837.

48. H. Chen, L. Wang and P. C. Li,"Nucleic acid microarrays created in the double-spiral format on a circular microfluidic disk", *Lab on a chip*, **2008**, 8, 826-829.

49. H. Hwang, Y. Kim, J. Cho, J. Y. Lee, M. S. Choi and Y. K. Cho,"Lab-on-a-disc for simultaneous determination of nutrients in water", *Analytical chemistry*, **2013**, 85, 2954-2960.

50. A. Bruchet, V. Taniga, S. Descroix, L. Malaquin, F. Goutelard and C. Mariet,"Centrifugal microfluidic platform for radiochemistry: Potentialities for the chemical analysis of nuclear spent fuels", *Talanta*, **2013**, 116, 488-494.

51. Y. Xi, E. J. Templeton and E. D. Salin,"Rapid simultaneous determination of nitrate and nitrite on a centrifugal microfluidic device", *Talanta*, **2010**, 82, 1612-1615.

52. M. C. Kong and E. D. Salin,"Spectrophotometric determination of aqueous sulfide on a pneumatically enhanced centrifugal microfluidic platform", *Analytical chemistry*, **2012**, 84, 10038-10043.

53. J. P. Lafleur, A. A. Rackov, S. McAuley and E. D. Salin,"Miniaturised centrifugal solid phase extraction platforms for in-field sampling, pre-concentration and spectrometric detection of organic pollutants in aqueous samples", *Talanta*, **2010**, 81, 722-726.

54. R. Gorkin, S. Soroori, W. Southard, L. Clime, T. Veres, H. Kido, L. Kulinsky and M. Madou,"Suction-enhanced siphon valves for centrifugal microfluidic platforms", *Microfluidics and Nanofluidics*, **2011**, 12, 345-354.

55. M. C. Kong and E. D. Salin,"A valveless pneumatic fluid transfer technique applied to standard additions on a centrifugal microfluidic platform", *Analytical chemistry*, **2011**, 83, 9186-9190.

56. M. C. Kong and E. D. Salin,"Pneumatically pumping fluids radially inward on centrifugal microfluidic platforms in motion", *Analytical chemistry*, **2010**, 82, 8039-8041.

57. K. Abi-Samra, L. Clime, L. Kong, R. Gorkin, T.-H. Kim, Y.-K. Cho and M. Madou,"Thermo-pneumatic pumping in centrifugal microfluidic platforms", *Microfluidics and Nanofluidics*, **2011**, 11, 643-652.

58. T. H. G. Thio, F. Ibrahim, W. Al-Faqheri, J. Moebius, N. S. Khalid, N. Soin, M. K. B. A. Kahar and M. Madou,"Push pull microfluidics on a multi-level 3D CD", *Lab on a chip*, **2013**, DOI: 10.1039/c3lc00004d.

59. S. Sadeghi, H. Ding, G. J. Shah, S. Chen, P. Y. Keng, C. J. Kim and R. M. van Dam,"On chip droplet characterization: a practical, high-sensitivity measurement of droplet impedance in digital microfluidics", *Analytical chemistry*, **2012**, 84, 1915-1923.

60. J. Hoffmann, L. Riegger, F. Bundgaard, D. Mark, R. Zengerle and J. Ducree,"Optical non-contact localization of liquid-gas interfaces on disk during rotation for measuring flow rates and viscosities", *Lab on a chip*, **2012**, 12, 5231-5236.

61. L. B. Pinheiro, V. A. Coleman, C. M. Hindson, J. Herrmann, B. J. Hindson, S. Bhat and K. R. Emslie,"Evaluation of a droplet digital polymerase chain reaction format for DNA copy number quantification", *Analytical chemistry*, **2012**, 84, 1003-1011.

62. D. A. Duford, D. D. Peng and E. D. Salin,"Magnetically driven solid sample preparation for centrifugal microfluidic devices", *Analytical chemistry*, **2009**, 81, 4581-4584.

63. J. Steigert, M. Grumann, T. Brenner, L. Riegger, J. Harter, R. Zengerle and J. Ducree,"Fully integrated whole blood testing by real-time absorption measurement on a centrifugal platform", *Lab on a chip*, **2006**, 6, 1040-1044.

64. M. Grumann, T. Brenner, C. Beer, R. Zengerle and J. Ducrée,"Visualization of flow patterning in high-speed centrifugal microfluidics", *Review of Scientific Instruments*, **2005**, 76, 025101.

65. S. C. Gifford, M. G. Frank, J. Derganc, C. Gabel, R. H. Austin, T. Yoshida and M. W. Bitensky,"Parallel microchannel-based measurements of individual erythrocyte areas and volumes", *Biophysical journal*, **2003**, 84, 623-633.

66. T. Herricks, M. Antia and P. K. Rathod,"Deformability limits of Plasmodium falciparum-infected red blood cells", *Cellular microbiology*, **2009**, 11, 1340-1353.

67. M. J. Pugia, G. Blankenstein, R. P. Peters, J. A. Profitt, K. Kadel, T. Willms, R. Sommer, H. H. Kuo and L. S. Schulman,"Microfluidic tool box as technology platform for hand-held diagnostics", *Clin Chem*, **2005**, 51, 1923-1932.

68. J. Gong and C. J. Kim,"All-electronic droplet generation on-chip with real-time feedback control for EWOD digital microfluidics", *Lab on a chip*, **2008**, 8, 898-906.

69. R. B. Paranjape, in *Handbook of Medical Image Processing and Analysis (Second Edition)*, ed. N. B. Isaac, Academic Press, Burlington, 2009, pp. 3-18.

70. K. Parulski and K. Spaulding, Boca Raton, FL: CRC Press, 2003, pp. 727-757.

71. M. Ĉadík,"Perceptual Evaluation of Color-to-Grayscale Image Conversions", *Computer Graphics Forum*, **2008**, 27, 1745-1754.

72. R. Szeliski, *Computer vision: algorithms and applications*, Springer, 2011.

73. E. Arias-Castro and D. L. Donoho,"Does median filtering truly preserve edges better than linear filtering?", *The Annals of Statistics*, **2009**, 37, 1172-1206.

74. D. L. Pham, C. Xu and J. L. Prince,"Current methods in medical image segmentation", *Annual review of biomedical engineering*, **2000**, 2, 315-337.

75. N. R. Pal and S. K. Pal,"A review on image segmentation techniques", *Pattern Recognition*, **1993**, 26, 1277-1294.

76. R. M. Haralick and L. G. Shapiro,"Image segmentation techniques", *Computer Vision, Graphics, and Image Processing*, **1985**, 29, 100-132.

77. J. Rogowska, in *Handbook of Medical Image Processing and Analysis (Second Edition)*, eds. N. B. Isaac and P. PhDa2 - Isaac N. Bankman, Academic Press, Burlington, 2009, DOI: http://dx.doi.org/10.1016/B978-012373904-9.50013-1, pp. 73-90.

78. N. Otsu,"A Threshold Selection Method from Gray-Level Histograms", *IEEE Transactions on Systems, Man, and Cybernetics*, **1979**, 9, 62-66.

79. F. Meyer,"Topographic distance and watershed lines", *Signal Processing*, **1994**, 38, 113-125.

80. L. Ding and A. Goshtasby,"On the Canny edge detector", *Pattern Recognition*, **2001**, 34, 721-725.

81. J. Canny,"A computational approach to edge detection", *IEEE transactions on pattern analysis and machine intelligence*, **1986**, 8, 679-698.

82. T. G. Smith Jr, W. B. Marks, G. D. Lange, W. H. Sheriff Jr and E. A. Neale,"Edge detection in images using Marr-Hildreth filtering techniques", *Journal of Neuroscience Methods*, **1988**, 26, 75-81.

83. D. Marr and E. Hildreth,"Theory of Edge Detection", *Proceedings of the Royal Society of London. Series B. Biological Sciences*, **1980**, 207, 187-217.

2. Instrumentation

2.1 Introduction

While centrifugal microfluidic platforms often share the common form factor of a compact-disc, there is much diversity in size, design features and fabrication methods across the field. To provide an effective solution to the need for precise volume measurements on CM platforms, a potential method must address this diversity by being applicable to as many platforms as possible. An image segmentation-based technique fits this profile suitably thanks to the lack of need for specialized equipment and the inclusion of digital cameras on most CM experimental setups. The development of this technique requires a set of evaluation CM platforms, an experimental apparatus used to operate the platforms and synchronized imaging instrumentation for the acquisition of real time platform images, all of which are presented in detail in this chapter.

2.2 Centrifugal Microfluidic Platforms for Method Evaluation

2.2.1 Overview of Microfluidic Fabrication Techniques

The initial trend in microfluidic platform fabrication was based on photolithography[1] applied to silicon-based substrates, a method borrowed from the manufacturing of integrated micro-electronic devices. Photolithography offers excellent reproducibility and high feature resolution while its use of silicon or glass as a substrate allows devices that possess flexible optical properties that are key

for spectroscopic applications. However, application of photolithography to microfluidic device fabrication requires the use of a clean room, construction of a lithographic mask for every new design and use of highly corrosive chemicals for etching.

A close relative is soft lithography[2, 3], which utilizes a single silicon mould created by photolithography to cast elastomeric polymers such as polydimethylsiloxane (PDMS). Polymer based devices greatly reduce fabrication time and cost while retaining essential optical properties. While the ability to create several devices from a single mould is an improvement, soft lithography suffers from similar drawbacks to photolithography. The fabrication of CM platforms through hot embossing of cyclic olefin copolymer (COC) using a mould created by photolithography has also been described[4]. Although hot embossing allows rapid replication of existing designs, a mould must still be created for every new design by lithographic means, which renders prototyping expensive in terms of time and cost.

The miniaturization of most everyday chemical analysis processes does not require the nanometer level of resolution given by photolithographic fabrication methods. The use of micrometer-scale structures remains firmly in the microfluidic domain while simplifying and accelerating the prototyping of microfluidic devices. Several rapid prototyping techniques are available that provide reproducible

features at the micrometer-scale using polymer substrates such as polycarbonate (PC) or polymethylmethacrylate (PMMA).

Laser based methods have been developed which include excimer laser ablation[5] and laser micromachining[6]. While effective at creating polymer-based microfluidic devices, laser fabrication techniques suffer from high power requirements and high instrumental costs.

A simple yet practical approach to rapid prototyping of microfluidic systems involves mechanical micromachining of device layers in a polymer substrate and assembly of device layers using pressure or thermally sensitive double-sided adhesive layers[7]. The adhesive layers simultaneously provide a bonding method along with high aspect ratio features provided by xurography[8], a technique commonly utilized in the advertising industry to cut graphics on adhesive films. This method allows the prototyping of microfluidic devices within just a few hours and using inexpensive components. Because of these powerful advantages, this method was chosen for the fabrication of the CM platforms described in the next section.

2.2.2 Centrifugal Microfluidic Platform Fabrication

Centrifugal microfluidic platforms were constructed in 5 layers (Figure 2-1) using transparent polycarbonate(PC) digital video disks (DVDs) (U-Tech Media Corporation, Taiwan) as a base substrate for the main platform layers

(Figure 2-1A,C,E) and double-sided adhesive (FLEXmount DFM-200-Clear V-95 150 poly V-95 400, FLEXCon, Spencer, MA, USA) for the bonding layers (Figure 2-1B,D). The individual layers were first designed using the Solidworks 2012 (Solidworks Corp., Concord, MA, USA) computer-aided design (CAD) program. The DVD layers were micro-machined using a four axis computer numerically controlled (CNC) milling machine (Modela MDX40, Roland Corporation, Japan) using a 700 μm diameter end mill for large scale features such as chambers and channels and a 1.59 mm diameter drill bit for vent and injection holes. The adhesive layers were cut by xurography with a cutting plotter (CE3000Mk2-60, Graphtec America, Inc., Santa Ana, CA, USA).

An alignment hole located on each layer was used to precisely align all layers of the platform together. Following assembly, all layers were pressed together using a cold laminator (Jet Mounter ML 25, Dryac, Concord, ON, Canada).

To enhance contrast during platform imaging and permit imaging of colourless substances, the middle DVD of every platform (Figure2-1C) was coated with matte black spray paint (Ultra Cover Painter's Touch, Rust-Oleum Corporation, Vernon Hills, IL, USA) before machining following experimentation using several commercial spray paints (Figure 2-2).

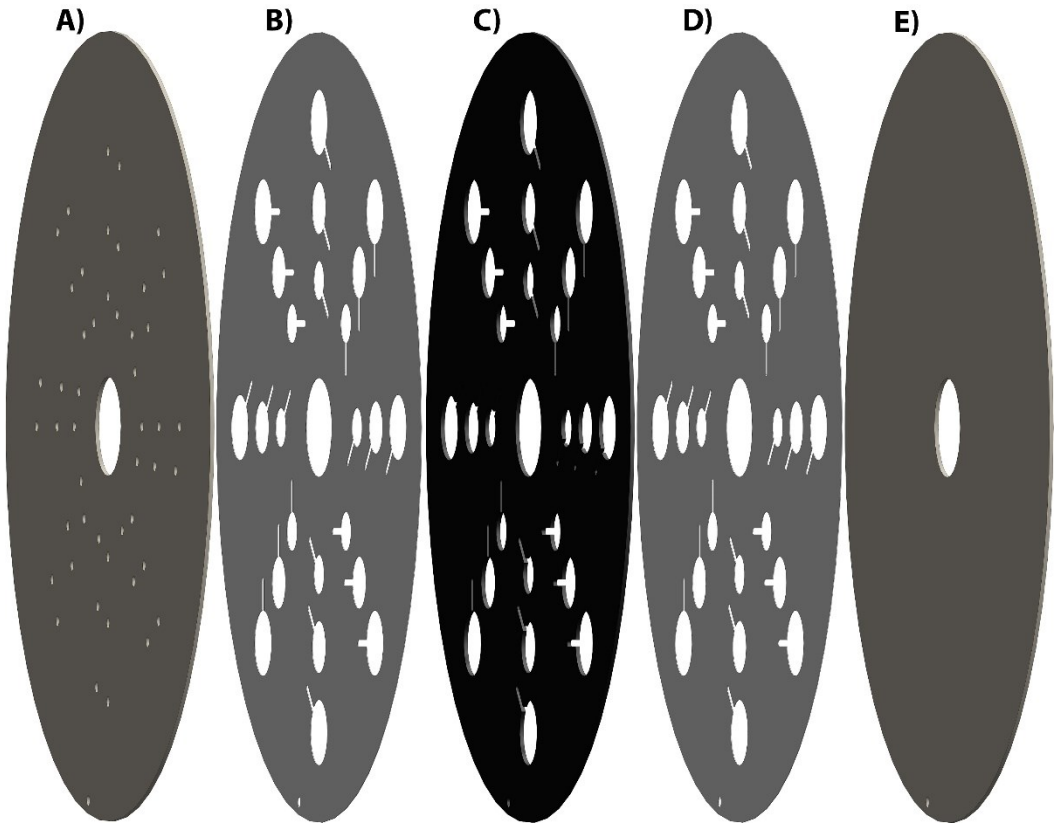

Figure 2-1: CM Platform layers. A) Top DVD layer containing drilled injection and vent holes. B) Double sided adhesive layer bonding layers A and C. C) Middle DVD layer containing chambers and channels. This DVD is spray-coated with black paint before machining to assist imaging contrast. D) Double sided adhesive layer bonding layers C and E. E) Bottom DVD layer.

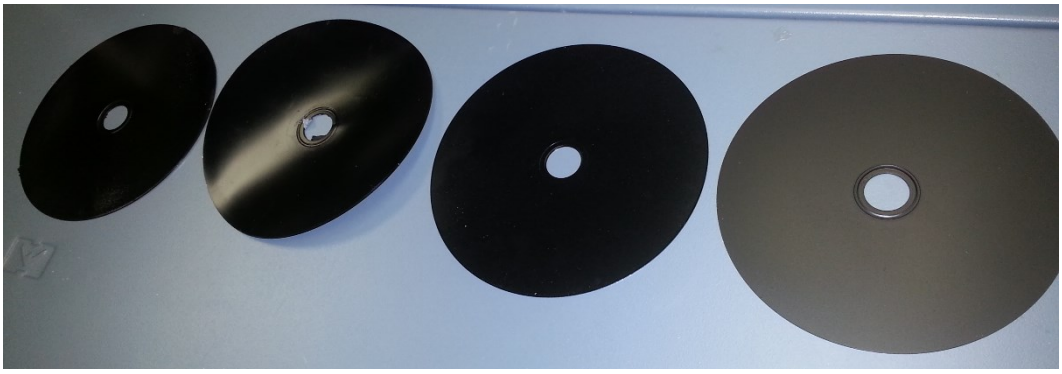

Figure 2-2: Evaluation of four brands of commercial spray paint (Left to right: Tremclad Rust Paint, Krylon Fusion, Rust-Oleum Glossy Plastic Specialty and Rust-Oleum Matte Ultra Cover Painter's Touch) applied to a DVD for enhancing imaging contrast. Oily residues can be seen on the Tremclad coated disk while the Krylon coating resulted in warping of the disk. The Rust-Oleum Ultra Cover paint was selected over the Speciality brand due to the matte surface it creates, a more even coating and faster drying.

The DVDs utilized for platform fabrication had a standard thickness of 600 μm while each double sided adhesive sheet had a thickness of 100 μm. This leads to an interior height of 800 μm for all platform chambers as they were milled through the full width of the central DVD layer. This height was used to estimate the volume of chambers during platform design.

2.2.3 Design of Platforms for Method Evaluation

Four different platform types (Figure 2-3) were designed to evaluate the effectiveness of the volume measurement technique for differently sized and shaped features. A platform consisting of eight identical wedges (Figure 2-3A) containing three circular chambers of varying radii (3, 4 and 5 mm) was constructed to conduct preliminary tests regarding the technique's precision and accuracy figures (Chapter 3). This platform was also utilized to evaluate the effect of a liquid's surface tension and colour on the effectiveness of the volume measurement technique (Chapter 4).

Three platforms containing chambers of equivalent areas with varying aspect ratios (1:1, 1:1.8, 1:2.3) and sizes were designed to verify the influence of feature shape on the precision of the volume measurement technique (Chapter 4). A platform comprised of sixteen identical wedges containing square chambers (Figure 2-3B) of varying sizes was used as a baseline for comparison with two platforms containing rectangles of varying aspect ratios (Figure 2-3C and D). The

areas of each same-sized square and rectangular chambers were designed to be equivalent to the area of the corresponding circular chamber in the previously described platform (28.27 mm^2, 50.27 mm^2, and 78.53 mm^2).

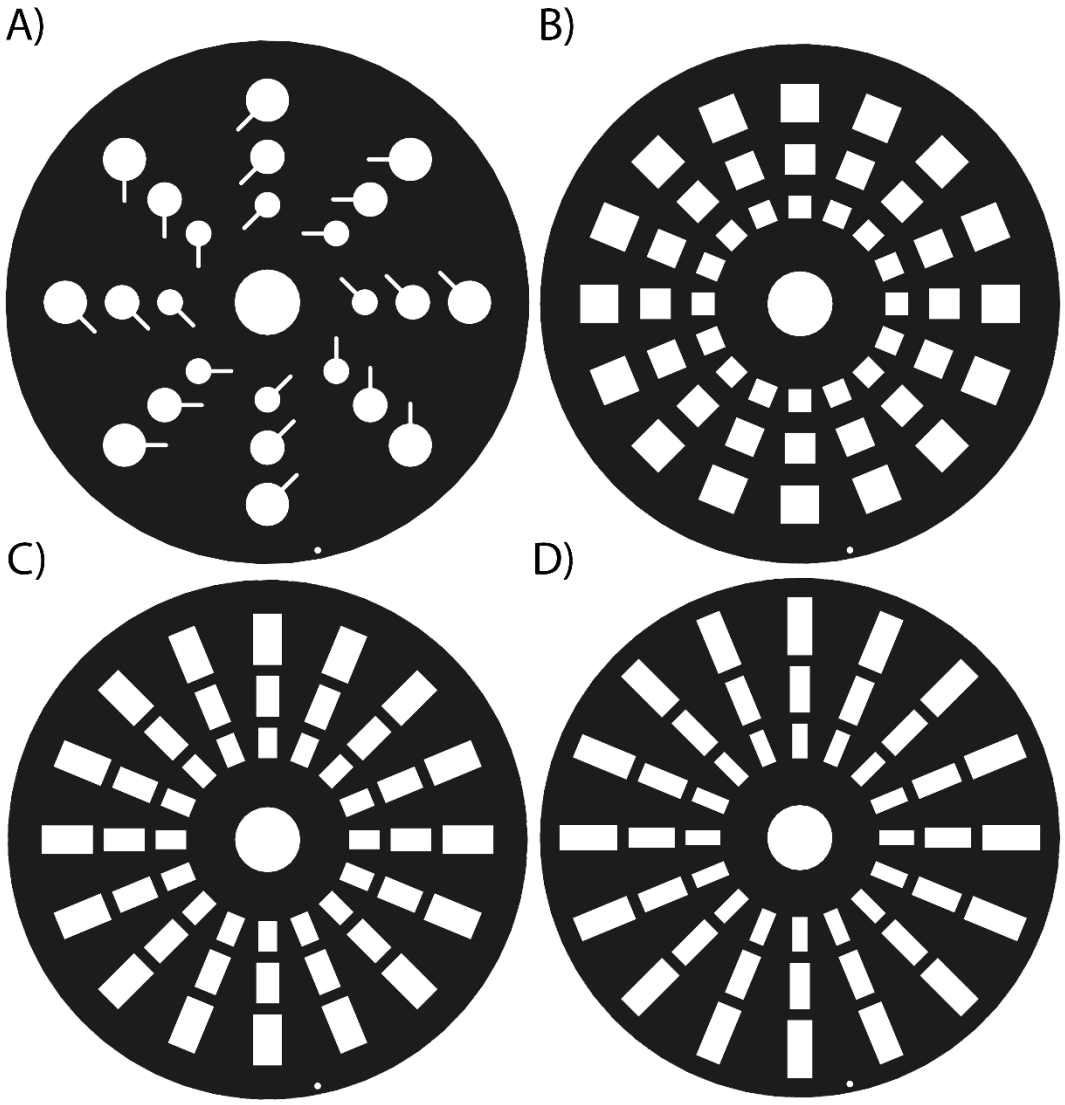

Figure 2-3: Four platforms utilized to evaluate the volume measurement technique presented in this thesis. A) Platform containing 8 wedges of different sized circular chambers (3, 4 and 5 mm radius). B) Platform containing 16 wedges of different sized squares with equivalent areas to platform A. C) Platform containing 16 wedges of different sized rectangles having a 1:1.8 aspect ratio with equivalent areas to platform B. D) Platform containing 16 wedges of different sized rectangles having a 1:2.3 aspect ratio with equivalent areas to platform A.

The initial circular chamber based platform included vents for every chamber to assist in liquid aliquot injection. Following experiments, this feature was considered unnecessary and was no longer included in the later platform designs.

2.3 Experimental Apparatus and Imaging System

2.3.1 Front-lit Stroboscopic Imaging System

Effective imaging of CM platforms in motion presents a unique challenge from an acquisition standpoint. Sharp images of moving objects require short integration times to obtain good resolution (*i.e.* avoid smearing). Conversely, bright and well contrasted images necessitate longer exposure or high intensity light sources. A balance between both of these aspects is key for the acquisition of high quality images for volume analysis by image segmentation.

An experimental apparatus previously described by Duford[9] was utilized as a starting point for the development of an effective imaging system (Figure 2-4A). This configuration consisted of a servomotor (Parker MPJ0922D3E-NPSN, Cadence Automatisation, Sainte-Thérèse, QC, Canada) and a servo drive (Parker AR-08AE, Cadence Automatisation) synchronized with a high-speed 24-bit colour digital camera (GRAS-14S5C-C, Point Grey Research Inc., Richmond, BC, Canada) and xenon arc strobe light (Shimpo DT-311A, Primo Instruments, Montreal, QC, Canada) via a custom LabVIEW program (LabVIEW 8.6, Developer Version, National Instruments, Vaudreuil-Dorion, QC, Canada). The camera was

placed at 90 degrees from the platform while the strobe light was positioned at an angle to illuminate the platform from the above without causing specular reflection. A white sheet of paper was added at the base of the motor spindle to produce a white background for imaging.

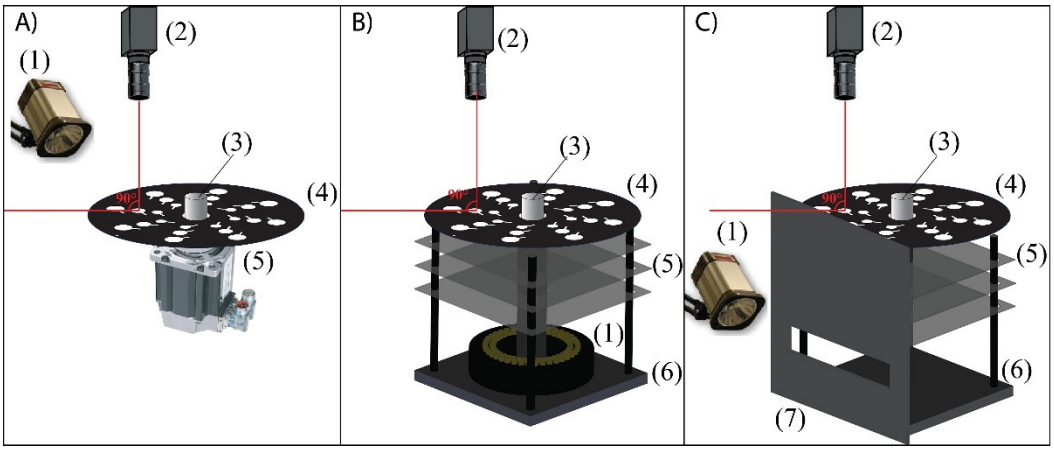

Figure 2-4: A) Original front-lit imaging system: 1) strobe light, 2) digital camera, 3) servomotor spindle, 4) CM platform and 5) servomotor base. B) Backlit LED ring light-based imaging system: 1) LED ring light, 2)-4) Same as A2-4, 5) diffusers and 6) support base. C) Backlit strobe-based imaging system: 1-4) Same as A1-4. 5) diffusers, 6) support base and 7) imaging aperture.

The operation of a CM platform on this system follows a simple protocol. First, the user inputs a list of rotational frequencies and a corresponding run-time for each frequency. The LabVIEW software then signals the servo drive to spin the servomotor at each indicated rotational frequency for the requested operating time. During rotation of the platform, a signal is sent to the strobe light and servomotor to trigger illumination of the platform and image acquisition every time the servomotor completes a full rotation (8000 steps). This signal can be adjusted to trigger every (8000 times y) steps to slow down the acquisition rate to once every

y rotations where *y* is an integer or every 8000 + *z* steps where *z* is an integer to cycle to a different spot on the platform during every rotation. For example, a trigger every 9000 steps will result in the platform rotating 405 (360 + 45) degrees between images, which provides a convenient way to sequentially image one eighth of the platform at a time during a single experiment without additional user input.

Images obtained from the front-lit imaging system presented a more than adequate contrast and sharpness for segmentation owing to the intense brightness of the strobe light, which allows the use of a short integration time. As such, this configuration was used for the initial measurements described in Chapter 3.

A side-effect witnessed during these experiments was the disappearance of the imaged meniscus of a liquid aliquot at the air-liquid interface (Figure 2-5A) if the CM platform wasn't precisely aligned to avoid specular reflection resulting from frontal illumination. Since segmentation of a liquid aliquot on an image requires a difference in intensity along the liquid-air interface, analysis of such images is impossible and requires re-imaging of the platform following manual repositioning, which complicates extended experiments. To optimize the acquisition process for the additional measurements presented in Chapter 4, additional systems were explored as discussed below.

Figure 2-5: CM platform injected with clear liquid imaged using three different imaging setups: A) Front-lit imaging system, B) Backlit LED imaging system, C) Backlit strobe imaging system.

2.3.2 Backlit LED Ringlight Imaging System

To improve the imaging process, a backlit system (Figure 2-4B) was constructed using an LED brightfield ringlight (S80-55, Schott North America Inc., Southbridge, MA, USA) linked to an externally triggered digital controller (MC1500, Schott North America Inc., Southbridge, MA, USA). The ringlight was placed on a polycarbonate support base located at the base of the motor spindle, which allows it to directly illuminate CM platforms from underneath.

This configuration brings three advantages. First, this allows imaging of the interior contents of a CM platform since the light hitting the platform from beneath can only pass through the coated middle DVD layer in locations where the disk was machined which corresponds to platform chambers. Second, the use of an LED-base light source allows for more reproducible lighting than a standard xenon-based strobe light where the use of an arc introduces a small amount of variability in light intensity. Third, a ring-based light source provides the opportunity for simultaneous imaging of a full platform under uniform lighting conditions. Taking

advantage of the third benefit requires camera optics that possess an appropriate working distance for imaging of a full platform while remaining close enough to capture sufficient light levels.

A series of diffusers (Figure 2-6) was mounted between the ringlight and the CM platform using four screws extending from the support base to create a uniform white imaging background. The diffusers were cut out of commercial artificial vellum paper with a cutting plotter and designed to match the base for easy modular assembly.

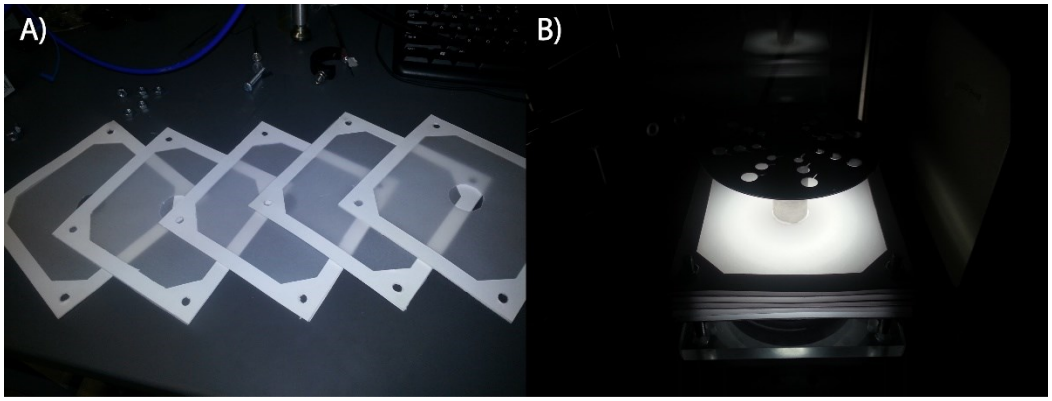

Figure 2-6: Diffusers used in the backlit ringlight imaging system. A) Image of five diffusive layers following fabrication. B) Image showing the diffusive layers mounted on the imaging system.

The diffusion of the ringlight was optimized by imaging a stationary CM platform filled with clear liquid while varying the number of mounted diffuser layers from none to 5 (Figure 2-7). It was expected that an increased number of diffusers would provide a more uniform background with the consequence of reducing the average lighting intensity. This factor was experimentally confirmed and an

appropriate level of lighting was reached with 5 diffusers, as can be seen on Figure 2-7F. This figure demonstrates a crisp image of the platform's interior with no visible background, achieving the desired conditions at a stationary level.

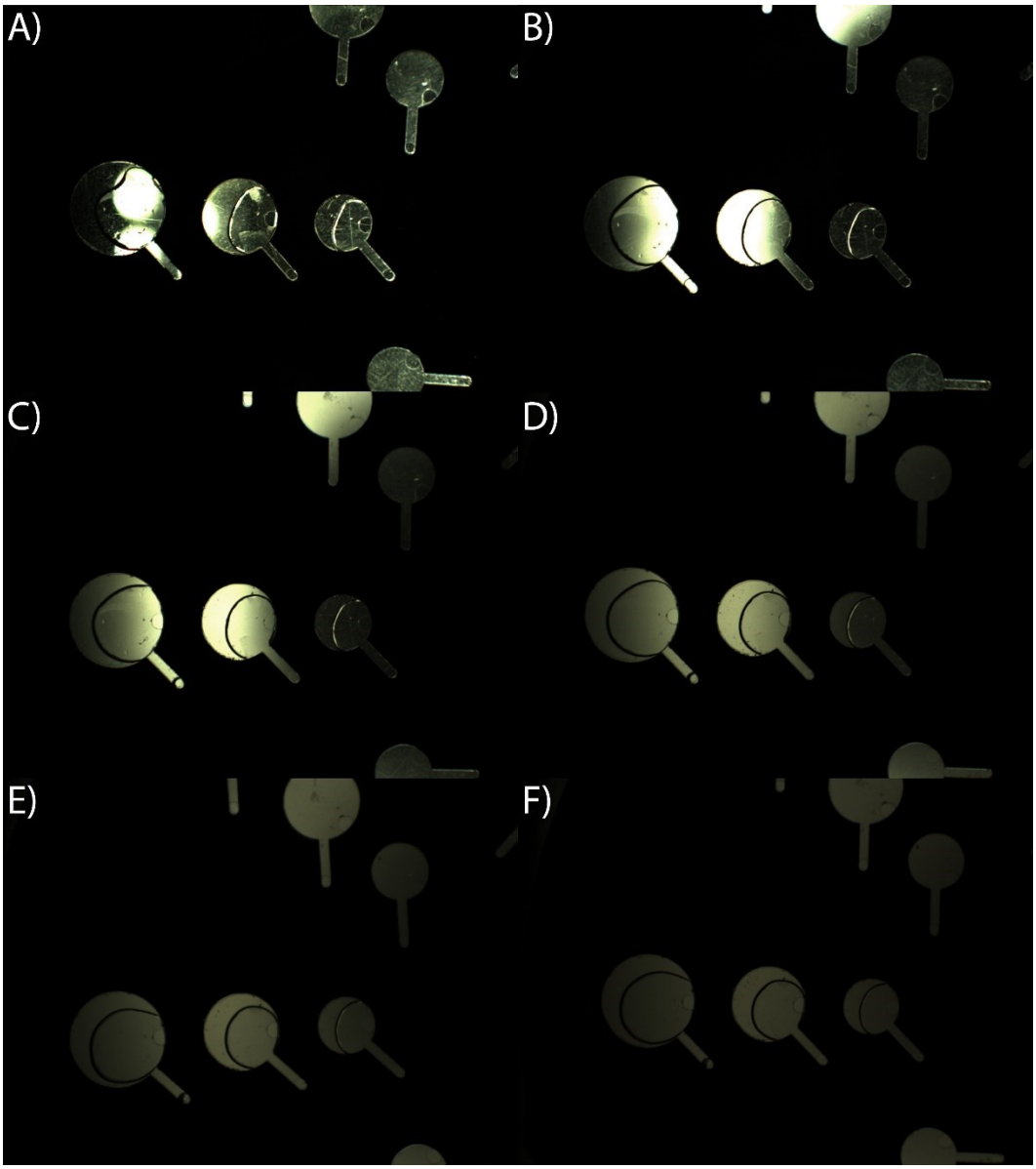

Figure 2-7: Images of a stationary CM platform containing a clear liquid and mounted on the backlit ringlight setup using: A) No diffuser B) One diffuser C) Two diffusers D) Three diffusers E) Four diffusers F) Five diffusers.

To image CM platforms in motion using this system, a custom MATLAB R2013B (The Mathworks Inc, Natick, MA, USA) program was utilized to load intensity and pulse duration settings to the ringlight controller and an external connection was extended from the servo drive to allow synchronized triggering of the ringlight alongside the digital camera using the methodology described in Chapter 2.3.1.

Various pulse durations were tested to balance light intensity with image sharpness. While the LED ringlight was capable of pulse durations down to 100 µs, such a setting produces insufficient light intensity for practical imaging purposes. A pulse duration of 200 µs shows a definite improvement while introducing a significant amount of blur (Figure 2-5B) when compared to the ~20 µs pulse duration of a xenon arc strobe light.

While a backlit ringlight imaging system shows significant potential for CM platform imaging by providing highly reproducible lighting conditions and eliminating background elements, the LED nature of the source demonstrates significant issues in terms of light intensity and pulse duration.

2.3.3 Backlit Stroboscopic Imaging System

From preliminary attempts, it was clear that an optimal system for platform imaging could be constructed by combining a backlit imaging stage with a xenon

arc strobe light (Figure 2-4C). To achieve a backlit configuration, the polycarbonate support base and diffusers from Chapter 2.3.2 were retained. One of the diffusers was placed directly on top of the support base to provide diffuse reflection of incoming light. A xenon arc strobe light was then positioned close to the servomotor spindle base and directed at the bottom diffuser layer to provide a bright spot of light underneath a mounted CM platform. To restrict the wide illumination angle of the strobe light and eliminate front illumination of the platform, a sheet of cardboard covered with aluminum foil with a rectangular aperture was positioned next to the servomotor base. Of the five diffusers used in Chapter 2.3.2, only three were necessary to diffuse the incoming light and provide a uniform white background for imaging.

The resulting configuration created a bright spot of light underneath the platform side closest to the aperture. While initial imaging was attempted directly above this spot, stray light in the form of specular reflection originating from the reflective metallic surface of the servomotor spindle resulted in poor image quality. This issue was accommodated by simply moving the camera to a location further away from the center of the light spot. Figure 2-5C displays an image acquired with this system of a CM platform containing a clear liquid. This figure demonstrates the superior characteristics for image segmentation possessed by images

acquired with this configuration, including a dark outline at the air-liquid interface, sharp edges, a lack of background signal as well as high intensity and contrast.

The backlit strobe-based imaging system was utilized for all experiments described in Chapter 4 to allow the rapid acquisition of high-quality platform images without the constraints displayed by the system described in Chapter 2.3.1.

2.4 References

1. S. Franssilla, *Introduction to Microfabrication*, Wiley, 1 edn., 2004.

2. J. C. McDonald, D. C. Duffy, J. R. Anderson, D. T. Chiu, H. Wu, O. J. Schueller and G. M. Whitesides,"Fabrication of microfluidic systems in poly(dimethylsiloxane)", *Electrophoresis*, **2000**, 21, 27-40.

3. D. C. Duffy, J. C. McDonald, O. J. Schueller and G. M. Whitesides,"Rapid Prototyping of Microfluidic Systems in Poly(dimethylsiloxane)", *Analytical chemistry*, **1998**, 70, 4974-4984.

4. J. Steigert, S. Haeberle, T. Brenner, C. Müller, C. P. Steinert, P. Koltay, N. Gottschlich, H. Reinecke, J. Rühe, R. Zengerle and J. Ducrée,"Rapid prototyping of microfluidic chips in COC", *J Micromech Microeng*, **2007**, 17, 333-341.

5. J. Kim and X. Xu,"Excimer laser fabrication of polymer microfluidic devices", *Journal of Laser Applications*, **2003**, 15, 255.

6. H. Klank, J. P. Kutter and O. Geschke,"CO(2)-laser micromachining and back-end processing for rapid production of PMMA-based microfluidic systems", *Lab on a chip*, **2002**, 2, 242-246.

7. H. Kido, J. Zoval and M. J. J. Madou,"Rapid Prototyping of Microfludic Systems", **2007**, 4, 101-105.

8. D. A. Bartholomeusz, R. W. Boutte and J. D. Andrade,"Xurography: rapid prototyping of microstructures using a cutting plotter", *Journal of Microelectromechanical Systems*, **2005**, 14, 1364-1374.

9. D. A. Duford, D. D. Peng and E. D. Salin,"Magnetically driven solid sample preparation for centrifugal microfluidic devices", *Analytical chemistry*, **2009**, 81, 4581-4584.

3. Volumetric Measurements by Image Segmentation: Basics and Characterization

3.1 Introduction

This chapter presents an image segmentation based method that was developed and characterized to perform volumetric measurements of liquids in CM platforms in motion. The method was designed to be as automated as possible to allow its applicability to the large variety of available design features that tend to be included on such platforms. Experiments have indicated a relative standard deviation (RSD) of 0.3% for replicate measurements and 1% for the same volume injected into different sized chambers. The versatility of the method should allow it to be used for a variety of applications including real time metering of volumes in platforms, quantitative monitoring of a design's performance in real time and the elimination of metering chambers in designs.

3.2 Basic Principles

Images of centrifugal microfluidic platforms provide the opportunity for precise analysis in two dimensions *(x,y)*. As volume measurement involves a third dimension, approximations regarding the platforms' height component *(z)* must be made for volumetric data to be obtained from CM platform images. Due to the fabrication method utilized (Chapter 2.2.2), the height of all chambers located on the same platform can be assumed to be equal (Figure 3-1A).

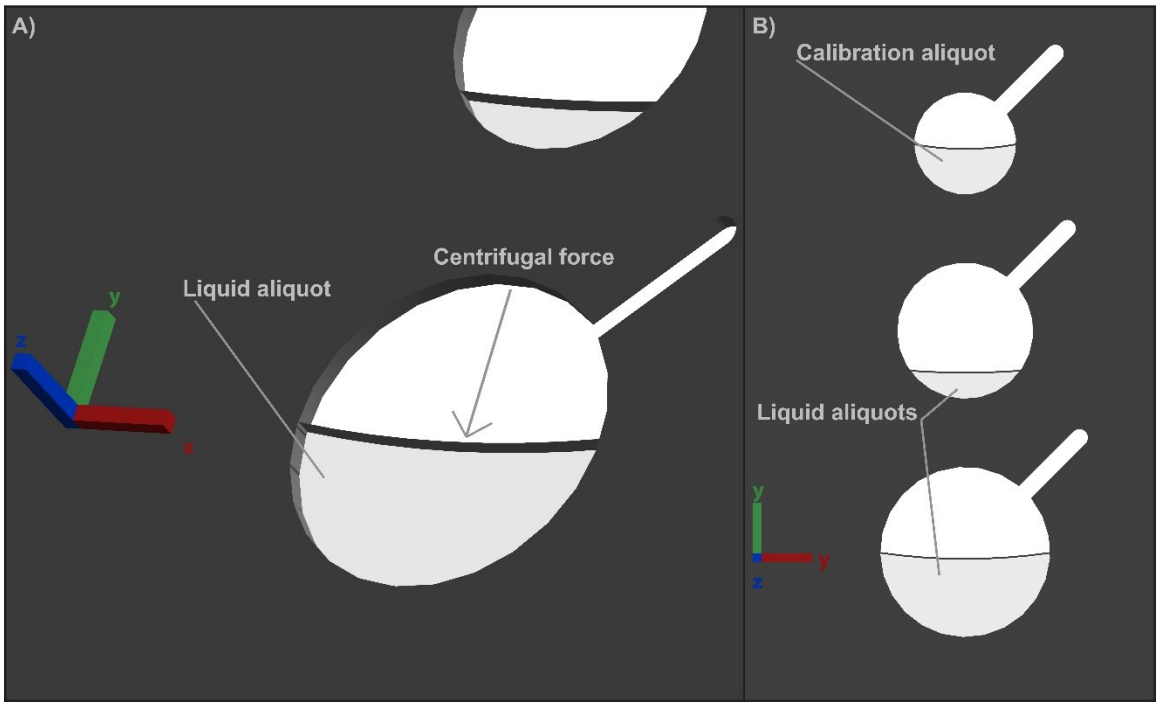

Figure 3-1: Demonstration of the assumptions enabling volume measurement by imaging A) 3-D Model of a liquid aliquot inside a CM platform in motion. The top and bottom layers are abstracted due to their transparent properties. Centrifugal force is shown flattening the meniscus. The height (z) is seen to be uniform across the platform. B) Model of an ideal image of a platform containing three liquid aliquots taken at 90 degrees. Black coating of the middle layer provides a sharp edge at the platform-liquid interface while the liquid meniscus provides an edge at the liquid-air interface due to change in refractive index.

In addition, the camera was placed at a 90 degree angle from the platform's surface, which completely eliminates the height component on images. (Figure 3-1B).

To obtain an accurate calibration without the need for z knowledge, a pre-metered aliquot injected into a calibration chamber must be employed as a reference. Using this configuration, the volume of liquids located inside any of the platform's chambers can be measured by considering it as approximately proportional to its area on images taken during the platform's operation

(Figure 3-2A). Areas for all liquids present on the platform can be easily obtained by image segmentation as they each form a closed outline when imaged inside a contrast-assisted platform (Figure 3-2B). A single calibration chamber containing a pre-metered aliquot can then be used to obtain direct volume readouts from a single image by ratioing its area with the areas of the liquid aliquots of interest (Figure 3-2C).

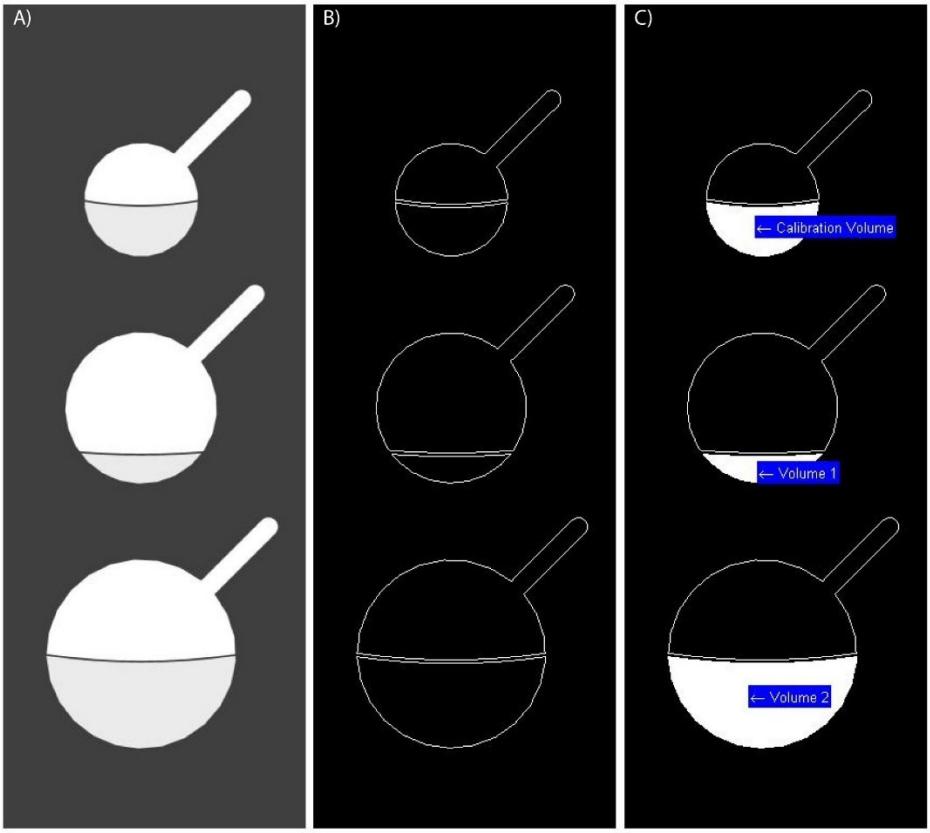

Figure 3-2: Basic principle of the volume measurement technique. A) Grayscale image of platform containing three liquid aliquots featured in Figure 3-1B. B) Image A segmented to locate the liquid aliquot outlines. C) Measurement of aliquot volumes by ratioing their area with that of a pre-metered calibration aliquot.

3.3 Image Processing Technique

3.3.1 Outline

The volumetric measurement technique can be separated into acquisition, enhancement, segmentation and measurement steps which are detailed in this section. A summary of the method applied to ideal and real platforms can be found on Figure 3-2. The technique was implemented using a graphical user interface (GUI) in MATLAB R2013B and its associated image processing toolbox. The description of this GUI can be found in Appendix A.

3.3.2 Image Acquisition

Experimental 24-bit colour images (Figure 3-3 A, B) were acquired with the front-lit stroboscopic imaging system described in Chapter 2.3.1. To keep the method applicable to any kind of liquid, independent of colour, the images were first converted from an RGB colour space to grayscale which retains only the luminance or brightness of the image (Figure 3-3 C, D).

It is important to note that 24-bit colour images consist of three channels of 8-bit information, resulting in only 8 bits of grayscale information or 256 possible intensity levels per pixel. This imposes limitations on edge-based segmentation

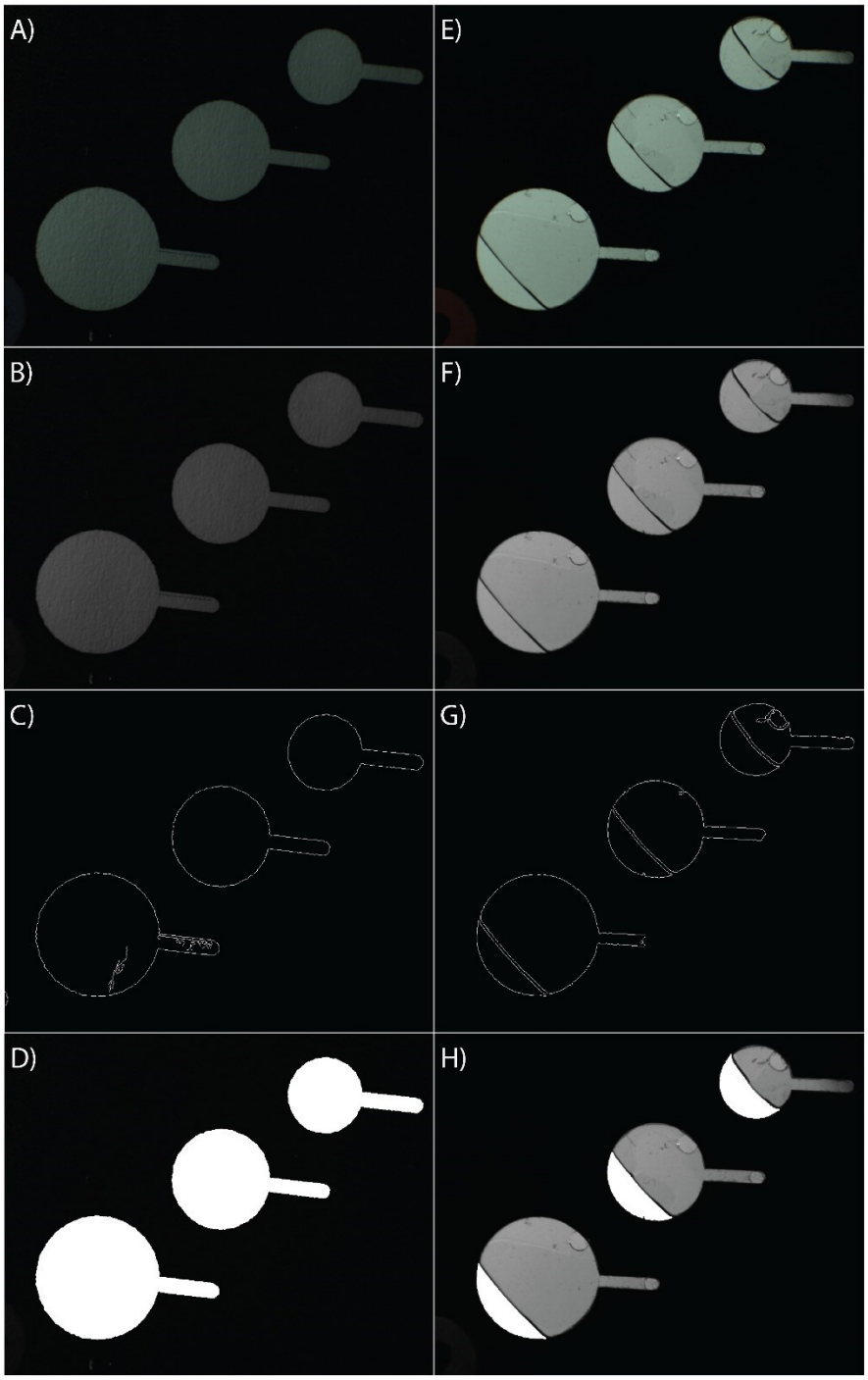

Figure 3-3: Overview of the steps of the volumetric measurement technique demonstrated on an ideal (A-D) and a real (E-H) platform. A) Raw image of an ideal platform. B) Conversion to grayscale to retain only the intensity information. C) Segmentation using the Laplacian-of-Gaussian operator. D) Area evaluation of user selected chambers after filling by morphological reconstruction. E)-H) Steps A-D performed on a real CM platform subsequent to injection of a 10 µL aliquot of distilled deionized water in each chamber.

that relies on differences in intensity. Since the intensity transitions at edges present on real images are not always sharp, a smaller number of bits per pixel can make precise localization of edges more difficult.

3.3.3 Image Enhancement

Several image enhancement techniques[1] can assist in the segmentation of platform images (Chapter 1.4.2) . Acquisition of images can be potentially noisy, which can introduce false edges during the segmentation process. Reduction of noise levels is best accomplished with the use of a median filter that can remove small amounts of noise while leaving edges intact due to its non-linear properties. Sharpening of image edges can be achieved through the application of an unsharp filter, while contrast can be improved through intensity adjustment to scale an intensity range of interest to the full available range.

Due to the high quality of the experimental images obtained by the imaging system, such enhancements were not deemed necessary prior to segmentation. However, each of the above mentioned image enhancement methods was implemented into the technique's GUI as an option.

3.3.4 Image Segmentation

Having obtained a sharp image of a CM platform and its contents, edge-based image segmentation[2-7] was performed to automatically partition the area occupied by all liquid aliquots located within the platform. Edge-based segmentation was

chosen due to its advantages when applied to contrast-assisted platforms containing a black surface layer. A liquid aliquot located inside such a platform presents a large change in intensity at both the liquid-platform and liquid-gas interfaces, regardless of platform design, rendering it ideal for edge-based segmentation.

Two edge-based segmentation techniques (Chapter 1.4.3.2) were evaluated for application in this step. Canny's method[3], based on the first order derivative of the image intensity, initially provided an accurate detection of the edge along the liquid-platform interface. However, it often suffered from poor performance at the junction of the liquid-platform and liquid-air interfaces on images with non-ideal contrast, resulting in missing edges due to a lack of sensitivity.

This issue was overcome by using the Laplacian-of-Gaussian (LoG)[8, 9] method which performs edge detection based on the second derivative of the image intensity. The LoG operator is the convolution of a discrete approximation to a Laplacian filter with a Gaussian filter. Its application first resulted in a light blurring of the image to reduce imaging noise and the possibility of flagging false edges. Since an edge is defined as a sharp transition in intensity, its first derivative will be shaped as a peak, and its second derivative will have a zero-crossing found at its location. However, given the discrete nature of pixels in an image, a real zero will often not be found for all edges. A decision was then made that the edge should

follow the negative peaks since this is the most conservative estimate. A binary image (Figure 3-3 E, F) of the edges was then traced by retaining only pixels with a second derivative value above a threshold based on the average second derivative value of the image. These edge pixels were flagged as *1's* in the segmented image, while background pixels were set to *0s*;

3.3.5 Area Measurement and Volume Readout

Following segmentation, closed or near-closed shapes were obtained for all liquid aliquots located on the image. A pixel was selected within the outline of each aliquot. The eight closest connected objects (*1's*) to this pixel were found by searching in both axial and diagonal directions and copied on a separate image. This process was followed by a bridging algorithm that connected *1's* that have a single *0* lying in between to prevent single pixel discontinuities. This resulted in a closed outline for all aliquots if it was not already the case.

The outline of each liquid aliquot was filled by morphological reconstruction[10] and all connected pixels were summed to obtain its area (Figure 3-3 D, H). The calibration aliquot is then selected by the user and its volume is indicated. The volume of each aliquot (L_{volume}) could then be computed by equation 3-1:

$$L_{volume} = \frac{C_{volume} \times L_{area}}{C_{area}}$$

Equation 3-1: Calculation of aliquot volume.

Where L_{area} is the area of the aliquot on the image, C_{area} is the area of the calibration aliquot on the image and C_{volume} is the volume of the calibration aliquot.

3.4 Experimental

3.4.1 Evaluation Platform Design and Fabrication

To characterize the volume measurement technique, a five layer evaluation platform was constructed in polycarbonate using a subtractive rapid prototyping method (Chapter 2.2.2).[11] This platform (Figure 3-4) consisted of eight identical wedges, each composed of three circular chambers (Radii of 3, 4 and 5 mm). The platform was designed to allow precision and accuracy measurements on pre-metered volumes injected into different sized chambers.

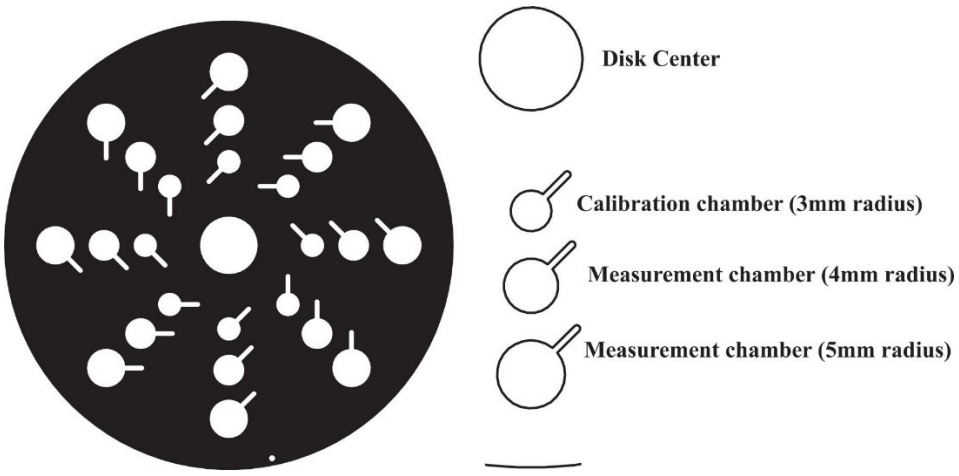

Figure 3-4: Design of the test platform. A full platform is shown on the left while the design of one of the platform wedges is shown on the right. Each platform contains eight identical wedges and is contrast enhanced by the addition of a black paint coating applied to the middle layer before machining.

3.4.2 Reagents

Distilled deionized water (DDW) was used to evaluate the technique. A clear liquid was utilized to demonstrate the applicability of this method to any liquid regardless of its colour. A small quantity of Triton-X (~0.03%) was added to solutions to reduce the surface tension of water, rendering the meniscus flatter and more reproducible.

3.4.3 Experimental Setup

An experimental apparatus containing a front illuminated imaging system was utilized as described in Chapter 2.3.1. All components of the system were synchronized using a custom LabVIEW interface[12] to allow the acquisition of 'still appearing' images of a CM platform while rotating. The magnification of the imaging system was set to be fully zoomed in on one wedge of the test platform at a time to give the best resolution possible.

3.4.4 Experimental procedure

An initial experiment was carried out to evaluate the imaging and image processing components of the system. An artificial "ideal" platform was constructed by printing a 1:1 design drawing of the test platform on paper and inserting it between two transparent DVDs to keep it flat. Eight wedges of the artificial platform were imaged five times each and the areas of each chamber were measured. An

RSD for area measurements between same-sized (Figure 3-5A) chambers was computed to determine a global imaging RSD.

The precision figure of the technique applied to real chambers was then determined by injecting a 10 µL aliquot of DDW into each chamber of a test platform with a 10.0 µL microsyringe (701 RN SYR, Hamilton Company, Reno, NV, USA). Six wedges of the platform were imaged separately for five replicate images each and the areas corresponding to each injected aliquot were measured. RSDs were calculated between areas for aliquots in same-sized chambers in different wedges (Figure 3-5A), between areas for aliquots located on the same wedge for different sized chambers (Figure 3-5B) and between imaging replicates for the same aliquot in time (Figure 3-5C). During the precision analysis, evaluation of several image processing parameters was conducted for method optimization. The standard deviation of the Laplacian-of-Gaussian operator was varied from 1.25 to 2 in steps of 0.25 and the effects of median filtering, image sharpening and contrast adjustment on method precision were assessed.

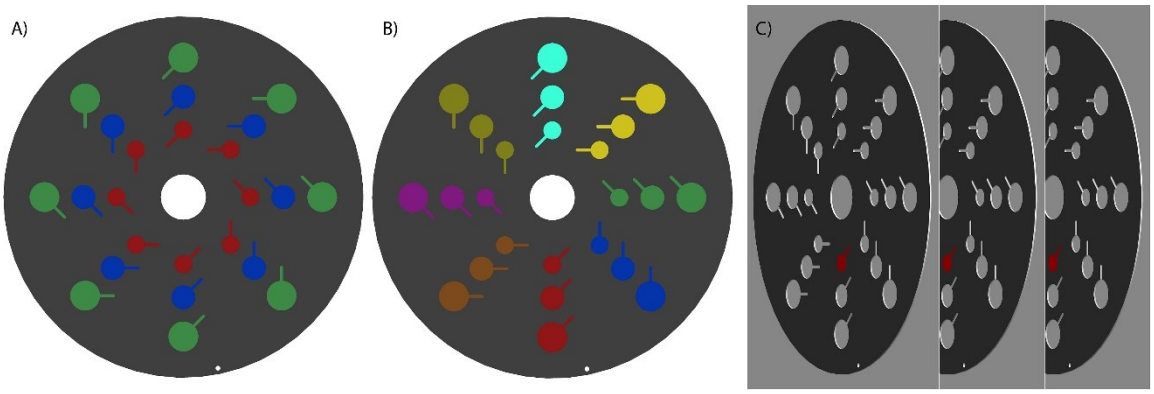

Figure 3-5: Colour representation of the measurements utilized for precision characterization experiments. A relative standard deviation was computed between all chambers of the same colour. A) Comparison of the same volume injected into same-sized chambers located on different wedges. B) Comparison of the same volume injected into different-sized chambers located on the same wedge. C) Comparison of the same aliquot between imaging replicates.

Finally, an accuracy experiment was conducted with two separate platforms to measure a series of injected volumes by ratioing their areas against a 10 µL calibration aliquot. All injections in this experiment were carried out with a 50.0 µL microsyringe (705 RN SYR, Hamilton Company, Reno, NV, USA). A 10 µL aliquot of DDW was injected into the calibration chamber of every wedge on both platforms. On the first platform, 20 µL and 40 µL were then injected respectively into the 4 and 5 mm radius measurement chambers. The same process was repeated for the second platform using 30 and 50 µL instead. Five wedges of each platform were imaged separately for five replicate images each and the areas of all liquids were measured. The final volume measurements were obtained by ratioing the areas of the experimental aliquots on a wedge against that of the calibration liquid located on the same wedge. A relative error on accuracy was

computed by comparing the experimental volumes obtained against the exact volumes injected. In addition, an RSD of the experimental volumes for each of the aliquots was calculated.

3.5 Results and Discussion

All precision and accuracy figures described in this section can be found in Table 3-1 and Table 3-2 respectively. As can be seen in Figure 3-A-D, the image processing technique was first applied to area measurements of the artificial platform. The RSD associated with the imaging and processing steps was computed from area measurements performed on each chamber of the platform and averaged over five images per chamber. This “ideal" imaging RSD was calculated to be 0.4% and found to be independent of chamber size at the magnification utilized for the experiment.

Table 3-1: Precision experiment data

Precision	RSD (%)
Ideal platform imaging	0.4
Real platform imaging	0.3
All chambers on a wedge	1
3 mm radius chambers	3
4 mm radius chambers	2
5 mm radius chambers	3

Table 3-2: Accuracy experiment data

Volume (μL)	Relative error on accuracy (%)	RSD (%)
20	2	1
30	2	1
40	4	1
50	3	4
Mean	3	2

Precision figures were obtained from measurements of 10 μL aliquots injected into every chamber of a test platform with an example measurement demonstrated in Figure 3-3 E-H. An experimental imaging RSD was initially calculated by evaluating the variations in area for the same liquid aliquot for five images per aliquot. This RSD was found to be 0.3%, which is very similar to the results obtained from the artificial platform experiment, demonstrating a high precision for the imaging and processing components of the technique.

RSDs were then calculated to characterize the variation of aliquot areas within the same wedge as well as between different wedges. First, an RSD was calculated for areas measured from aliquots injected into different sized chambers located on the same wedge and averaged over five images. This RSD was found to be 1% and appears to be limited by the precision of the syringe used to perform the injections, which has a manufacturer established precision of 1% per injection

at 80% of the barrel capacity (i.e. roughly 0.08 μL). RSD values were then calculated for areas of aliquots injected into same-sized chambers in six different wedges and averaged over five images per wedge. These RSDs were found to be roughly 3% and did not appear to vary with chamber size. This variability appears to be caused by the irreproducibility of the strobe light illumination during platform operation. This irreproducibility causes a variation of 1% in the intensity profile of the images of the different wedges. The precision figures obtained from this experiment demonstrate the need for a calibration chamber located on the same image as a measured aliquot to act as reference in order to obtain the best precision possible. While a calibration chamber occupies a small amount of platform real estate, only a single chamber of this type is required to obtain measurements of multiple aliquots located on the same image. This results in less platform real estate being required when compared to the multiple metering chambers that would be necessary for an equivalent measurement.

Accuracy figures were computed following the measurement of pre-metered aliquots (20, 30, 40 and 50 μL) on two test platforms. Each wedge of the platform contained its own calibration chamber in which a 10 μL aliquot of DDW was injected as a calibration standard. The areas of the two pre-metered aliquots per wedge were measured, ratioed against the calibration liquid to obtain their volumes and averaged over five images per wedge for five wedges. The mean relative error

between the injected and experimental volumes was found to be on the order of 3%. This error could be explained by a variation in the imaged appearance of the meniscus for liquids at different radial positions. Careful observation of the image of the meniscus at the air-liquid interface (Figure 3-3H) shows a variation in thickness most likely caused by a minute difference in alignment of the platform within the field of view of the camera. As the segmentation step relies on a closed outline, only the inner side of the meniscus is included, creating an offset in area that depends on the thickness of the meniscus image. A linear calibration model (Figure 3-6) of measured volumes against injected volumes showed excellent linearity (R^2 = 0.9997) and a standard error of prediction of ~0.2 µL, indicating that such a model can easily correct this offset. In addition, measurement chambers can be designed that reduce this effect by decreasing the size of air-liquid interfaces.

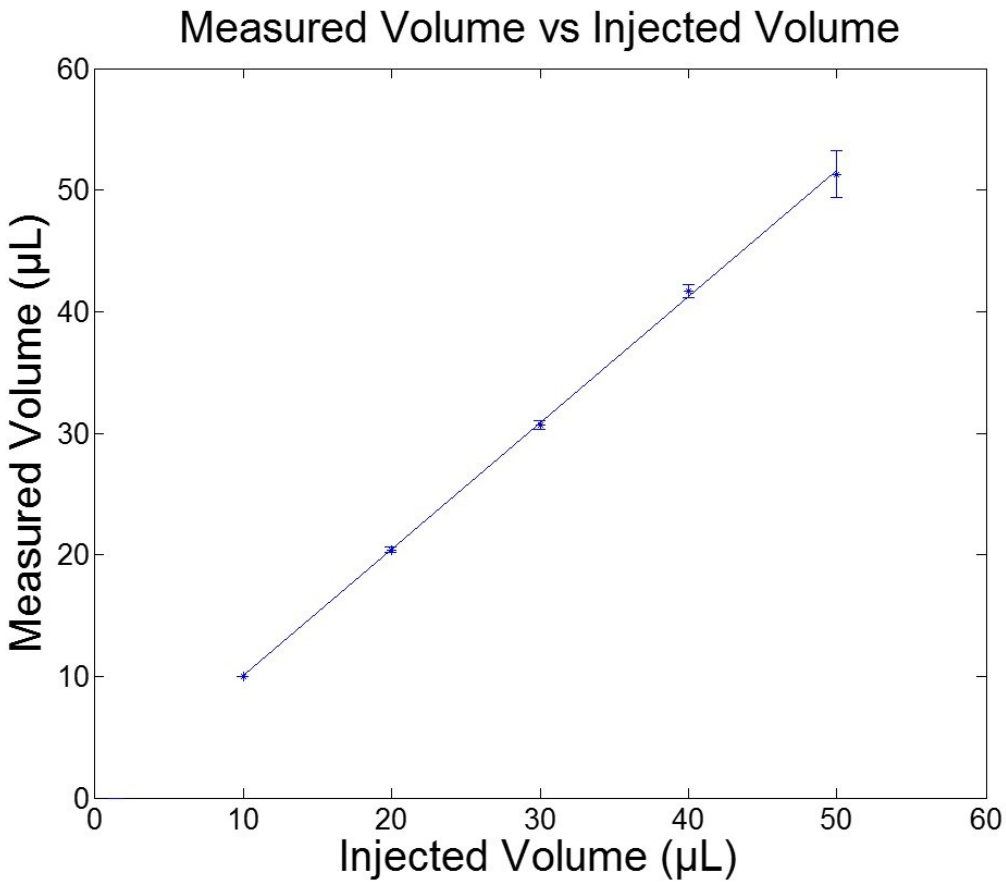

Figure 3-6: Volume measured by the image processing technique vs volume injected with a 50 µL syringe.

Optimal use of the Laplacian-of-Gaussian segmentation technique requires the appropriate selection of a standard deviation for the LoG operator. A larger standard deviation provides a greater amount of blur which results in an error in the localization of true edges. A smaller standard deviation results in less blur, which could cause missing edge pixels and an increased amount of false edges due to heightened noise. To empirically confirm this relationship, the influence of the LoG operator standard deviation was verified for optimal precision using the data obtained for aliquots in different-sized chambers located on the same wedge.

A standard deviation of 1.25 resulted in significant error (31%) due to the inability of the segmentation to form closed outlines on some images. For standard deviations of 1.5, 1.75 and 2, precision figures varied only at the third decimal: 1.27%, 1.28% and 1.34% respectively. While it did not impact significantly on method performance, this decrease in precision was expected as increased blurring caused by a larger standard deviation has an impact on the localization of the true edge of the liquid meniscus, which has an adverse effect on precision.

The effects of several enhancement techniques including median filtering, contrast enhancement and unsharpening of the images were explored to help reduce noise in the images and increase the intensity difference at edges to improve segmentation. It was found through the precision experiment data that the best precision was obtained without any enhancement. This suggests that the majority of the variation in measurements is caused by experimental injection error as there is little contribution from the processing itself.

The use of edge-based segmentation in a grayscale colour space combined with contrast-assisted platforms should render this technique applicable to liquids of any colour and transparency, as demonstrated by the use of DDW in experimental measurements. This aspect is highly valuable for use on CM platforms given their versatility in the type of samples that can be pumped.

3.6 Conclusions

An image-segmentation based volume measurement technique was developed and demonstrated to be an effective tool for volume measurements. Edge-based segmentation should make this technique applicable to a variety of design features as it has been shown to be unaffected by feature size. Direct volume measurements offer the potential for the development of CM analytical methods that require precise volume knowledge without the need for metering chambers, saving valuable real estate on CM platforms. Such measurements should allow the evaluation of new design features directly and quantitatively through real time flow monitoring. The ability to measure volumes without relying on discrete introduction via metering chambers could be highly valuable for use in continuous-flow platforms[13] where such introduction may not be desirable. The demonstrated technique is versatile, flexible towards the needs of experimenters and does not require any additional components beyond those included on a typical CM experimental apparatus.

3.7 References

1. R. B. Paranjape, in *Handbook of Medical Image Processing and Analysis (Second Edition)*, ed. N. B. Isaac, Academic Press, Burlington, 2009, pp. 3-18.

2. L. S. Davis,"A survey of edge detection techniques", *Computer Graphics and Image Processing*, **1975**, 4, 248-270.

3. J. Canny,"A computational approach to edge detection", *IEEE transactions on pattern analysis and machine intelligence*, **1986**, 8, 679-698.

4. L. Ding and A. Goshtasby,"On the Canny edge detector", *Pattern Recognition*, **2001**, 34, 721-725.

5. S. Lakshmi and D. V. Sankaranarayanan,"A study of Edge Detection Techniques for Segmentation Computing Approaches", *International Journal of Computer Applications*, **2010**, CASCT, 35-41.

6. S. Bhardwaj and A. Mittal,"A Survey on Various Edge Detector Techniques", *Procedia Technology*, **2012**, 4, 220-226.

7. N. R. Pal and S. K. Pal,"A review on image segmentation techniques", *Pattern Recognition*, **1993**, 26, 1277-1294.

8. D. Marr and E. Hildreth,"Theory of Edge Detection", *Proceedings of the Royal Society of London. Series B. Biological Sciences*, **1980**, 207, 187-217.

9. T. G. Smith Jr, W. B. Marks, G. D. Lange, W. H. Sheriff Jr and E. A. Neale,"Edge detection in images using Marr-Hildreth filtering techniques", *Journal of Neuroscience Methods*, **1988**, 26, 75-81.

10. P. Soille, *Morphological Image Analysis: Principles and Applications*, Springer-Verlag New York, Inc., 2003.

11. H. Kido, J. Zoval and M. J. J. Madou,"Rapid Prototyping of Microfludic Systems", **2007**, 4, 101-105.

12. D. A. Duford, D. D. Peng and E. D. Salin,"Magnetically driven solid sample preparation for centrifugal microfluidic devices", *Analytical chemistry*, **2009**, 81, 4581-4584.

13. A. P. Bouchard, D. A. Duford and E. D. Salin,"Non-contact addition, metering, and distribution of liquids into centrifugal microfluidic devices in motion", *Analytical chemistry*, **2010**, 82, 8386-8389.

4. Extended Method Characterization

4.1 Introduction

In Chapter 3, image segmentation of platform images was demonstrated to produce precise and accurate volumetric measurements for distilled deionized water aliquots located inside CM platforms in motion. To establish the broad applicability of this technique, this chapter explores image segmentation's precision in response to common experimental parameters. A study of edge localization using artificial "ideal" platforms was conducted to investigate the impact of optical magnification. The applicability of the technique to liquids of various colours was demonstrated using dyes of primary (red, yellow and blue) and secondary (orange, purple and green) colours. As solvents other than water may be of interest in many analytical applications, the precision of the technique was characterized following its application to aliquots of solvents with varying surface properties. To illustrate the versatility of the technique in regards to chamber shape, a study was conducted using chambers of varying aspect ratios. The influence of platform rotational frequency was also investigated as the ability to conduct volume measurement independent of rotational frequency is of great interest to CM experiments. The experiments presented in this chapter demonstrate the flexibility of the volume measurement technique and its potential for easy integration into CM techniques.

4.2 Parameter Selection

4.2.1 Optical Magnification

Basic imaging of CM platforms in-motion requires only a digital camera and stroboscopic light. These are inexpensive components present in many CM laboratories for visual evaluation of platform designs[1]. Given the wide range of volumes that can be handled by CM platforms, some setups may also present telescopic lenses or even microscopes[2] for magnification and enhanced visualization. To ensure applicability across various experimental setups, the effect of optical magnification should be explored.

4.2.2 Liquid Colour

Analytical processes often employ spectroscopic detection techniques that allow for precise determinations. Such determinations have successfully been implemented on CM platforms[3-5]. As spectroscopic analyses often employ brightly coloured analytes, successful image-based volume measurements of such compounds must be flexible in regards to analyte colour. This flexibility is also required by bio-medical analyses that are often performed on whole blood samples[6, 7]. Generalization of the applicability of the volume measurement technique to coloured samples requires an investigation of the influence of liquid colour on technique precision.

4.2.3 Liquid Surface Properties

While many analytical procedures make use of aqueous solutions of samples, certain sample preparation methodologies require the use of organic solvents[8, 9] or high concentrations of detergents[10]. The varying surface properties of these liquids present an additional challenge to the volume measurement technique given the predominance of surface forces at the microfluidic scale[11].

As the technique relies on an edge at the air-liquid-polymer interface due to refractive index changes, liquid properties which influence meniscus formation and thickness must be investigated. Of interest in this topic are intermolecular interactions within the liquid as well as interactions between the liquid and the polymer substrate that forms the centrifugal microfluidic platform.

The cohesiveness of liquid-liquid molecule interactions can be represented by the liquid's surface tension (γ) measured at an interface, most commonly against air (γ_{la}). The meniscus generated at the air-liquid-polymer interface is the result of the balance of cohesive forces between liquid molecules and attractive forces between liquid molecules and the polymer surface. This interface can be characterized by the contact angle (θ_c) presented at the meniscus, which can be modelled by Young's Equation (Equation 4-1)[12].

$$\cos\theta_c = \frac{\gamma_{sa} - \gamma_{sl}}{\gamma_{la}}$$

Equation 4-1: Contact angle of a liquid drop on an ideal solid surface

where γ_{sa} is the surface tension at the solid-air interface, γ_{sl} is the surface tension at the solid-liquid interface and γ_{la} is the surface tension at the liquid-air interface. As such, substitution of a liquid other than water will result in a change in contact angle via γ_{sl} and γ_{la}, affecting meniscus shape. As γ_{la} can be more readily measured than γ_{sl}, the effect of surface properties on the precision of the volumetric measurement technique should be evaluated using substances with varying air-liquid surface tensions.

4.2.4 Aspect Ratio

Centrifugal microfluidic features come in varying shapes and sizes depending on the application in question[13, 14]. Ideally, edge-based segmentation applied to contrast-enhanced centrifugal microfluidic platforms should provide a solution for volumetric measurements independent of design feature size or shape. While size independence of method precision was previously established for circular platforms (Chapter 3), alternative shapes must be explored. Segmentation of chamber outlines is readily accomplished because of the black surface coating of the platform's middle layer, which suggests that the main variation in measurements between different chamber shapes is the length of meniscus that must be segmented. Rectangular shapes of constant area with varying aspect ratios provide an easy method for the determination of this variation.

4.2.5 Rotational Frequency

Miniaturization of analytical processes into CM platforms requires precise flow control to ensure the completion of each unit operation before continuing to the next. This process is most commonly accomplished through the use of capillary burst valves that pin the meniscus in a channel of smaller cross sectional area until sufficient centrifugal force is provided to permit the liquid to expand (or burst) into a channel of larger cross sectional area[15]. The pressure required for the liquid to burst through such a valve (P_b) is defined by Equation 4-2[14].

$$P_b = \frac{4\gamma sin\theta_c}{D_h}$$

Equation 4-2: Burst pressure for a liquid inside a capillary burst valve

where γ is the liquid surface tension, θ_c is the contact angle at the liquid/valve interface and $D_h$is the hydraulic radius of the valve. In turn, the centrifugal pressure (P_ω) exerted on a liquid inside a rotating centrifugal microfluidic platform can be found in Equation 4-3[16].

$$P_\omega = \rho\bar{r}\Delta r\omega^2$$

Equation 4-3: Pressure exerted on a liquid by centrifugal force

where ρ is the liquid density, $\bar{r}$ is the average radial distance of the liquid, Δr is the length of the liquid body and ω is the rotational frequency. Liquid flow then occurs when $P_\omega \geq P_b$. A flow control scheme that utilizes capillary burst valves requires that each consecutive valve be more restrictive to liquid flow than the previous so that they may be opened sequentially through ramping of the

platform's rotational frequency. In order to quantitatively monitor liquid flow during each unit operation, it is important that the volume measurement technique utilized be applicable to a wide range of rotational frequencies. As image segmentation based volume measurements rely on a closed outline formed by the liquid-platform and liquid-air interfaces, the influence of rotational frequency on the shape and thickness of the meniscus at the liquid-air interface must be investigated.

4.3 Experimental

4.3.1 Evaluation Platform Design and Fabrication

Four evaluation platform designs (Figure 4-1) were created to conduct the experiments described in this chapter (Chapter 2.2.3). Each platform consisted of five layers that were fabricated using a subtractive rapid prototyping technique described in Chapter 2.2.2[17]. A platform (Figure 4-1A) containing eight identical wedges of three circular chambers of varying radii (3,4 and 5 mm) was constructed for experiments involving the effect of coloured analytes and liquid surface properties. Three additional platforms were designed to evaluate the influence of feature shape and aspect-ratio on the precision of the volume measurement technique. Each of these platforms contained a set of sixteen wedges of rectangular chambers having areas identical to those of the circular chambers (28.27 mm^2, 50.27 mm^2, and 78.53mm^2) with varying aspect ratios (1:1, 1:1.7,

1:2.3) (Figure 4-1 B-D). The middle layers of all platforms were spray-painted with a black contrast layer to assist in segmentation.

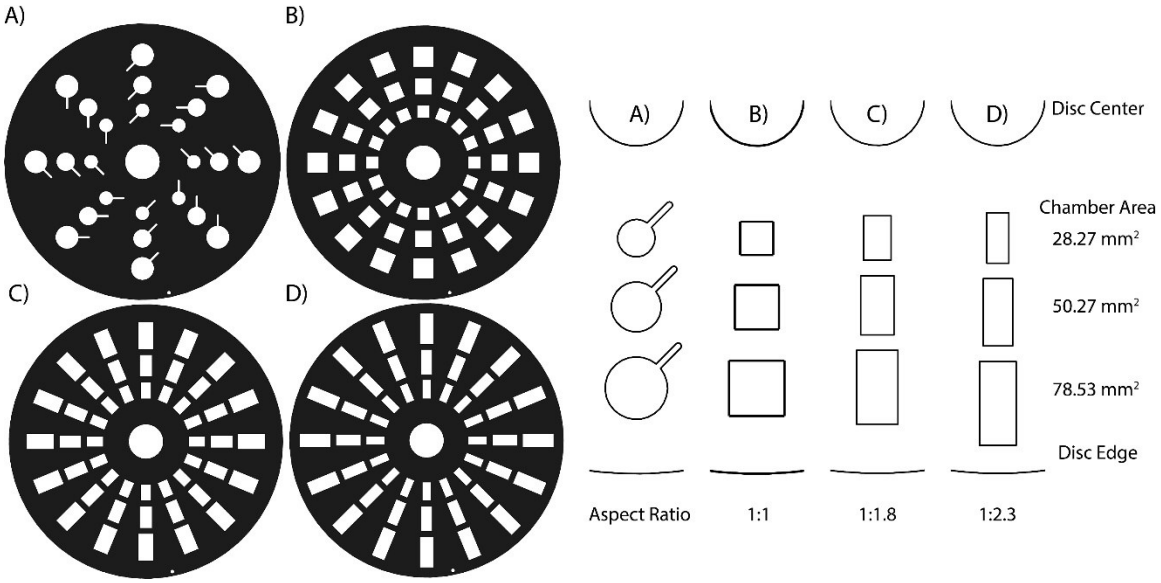

Figure 4-1: Design of test platforms. Each platform was contrast enhanced by the addition of a black paint coating applied to the middle layer before machining. A) 8 wedge platform containing circular chambers of varying radii (3,4,5 mm). B)-D) 16 wedge platforms containing rectangular chambers of varying aspect ratios (1:1, 1:1.8 and 1:2.3) with same areas as chambers of platform A.

4.3.2 Reagents

Characterization of the method response to coloured analytes was conducted using commercial food colouring. Solutions of three primary colours (red, blue and yellow) were prepared in distilled deionized water (DDW) and mixed in equal proportions to obtain three secondary colours (orange, purple and green). Experiments involving feature shape and rotational frequency were conducted using DDW. A small amount of Triton-X (0.03%) was added to all aqueous solutions to make the meniscus more reproducible by reducing the surface tension

of water. Investigation of the effect of surface properties was conducted using pure hexadecane (Caledon Laboratories Ltd., Georgetown, ON, Canada), ethylene glycol, methanol and ethanol (Sigma-Aldrich Canada Co., Oakville, ON, Canada).

4.3.3 Experimental Setup

An experimental apparatus featuring a stroboscopic backlit imaging system described in Chapter 2.3.3 was employed to acquire still-appearing platform images for all experiments performed in this chapter. Each platform was imaged one wedge at a time to ensure the best resolution possible for platform images.

4.3.4 Image Processing

The volumetric measurement technique evaluated in this chapter was described in Chapter 3 and utilized without modification. The technique was implemented via a graphical user interface developed using MATLAB R2013B and its associated image processing toolbox.

4.3.5 Experimental Procedure

The dependency of image segmentation reproducibility on optical magnification was determined using an artificial “ideal” platform consisting of a 1:1 design drawing of the platform featured in Figure 4-1A. As the dial of the lens attached to the digital camera did not feature any markings regarding zoom level outside of the minimum (1X) and maximum (10X), platform images were taken at 1X, 10X and three intermediary settings that were calibrated using platform images. To

avoid disturbing the experimental setup, the camera was focused at the radial position of the 5 mm radius chambers when zoomed in and kept at the same position for all images. Eight platform wedges were imaged five times each. Platform images were segmented and the area for the 5 mm radius chambers was computed for each wedge to obtain a relative standard deviation (RSD) for each zoom level.

An application of the volume measurement technique to six coloured solutions (red, blue, yellow, orange, purple, green) was demonstrated using a test platform (Figure 4-1A). A 50 µL aliquot of each coloured solution was injected into separate 5 mm radius chambers using a 50.0 µL microsyringe. To calibrate these measurements, a 10 µL aliquot was injected into corresponding 3 mm radius chambers with a 10.0 µL. All chambers were sealed using double-sided adhesive film to avoid evaporation of aliquots. Figure 4-2 shows a picture of the platform before operation. Each coloured aliquot was imaged five times at a rotational frequency of 1200 RPM and processed to obtain a volume. An RSD between the volumes obtained for each aliquot was then computed.

Figure 4-2: Picture of the colours analysis platform.

To explore the influence of liquid surface properties on the performance of the volume measurement technique, experiments were conducted using 10 µL aliquots of organic solvents injected into every chamber of a test platform (Figure 4-1A). Separate platforms were utilized for each of the tested solvents: ethylene glycol, hexadecane, methanol and ethanol. Each of the eight platform wedges was imaged five times at a rotational frequency of 1200 RPM, immediately after injection into and sealing of wedge chambers to avoid solvent evaporation. The areas for all liquid aliquots were then measured and an RSD was calculated between areas for aliquots located on the same image. The process was repeated to obtain RSDs for each solvent.

The effect of design feature shape and aspect ratio on method precision was investigated using the three platforms shown on Figure 4-1 B-D. Aliquots of 10 µL of DDW were injected into every chamber of each platform. All chambers were sealed with double sided adhesive film immediately after injection to avoid volume loss due to evaporation. Figure 4-3 demonstrates the filled rectangular 1:1:8 aspect ratio test platform prior to imaging. Each of the sixteen wedges of a platform was imaged five times at a rotational frequency of 1200 RPM and areas were computed for every aliquot. An RSD was then calculated for aliquots located in different-sized chambers on the same wedge for each of the platforms to obtain an RSD for every aspect ratio.

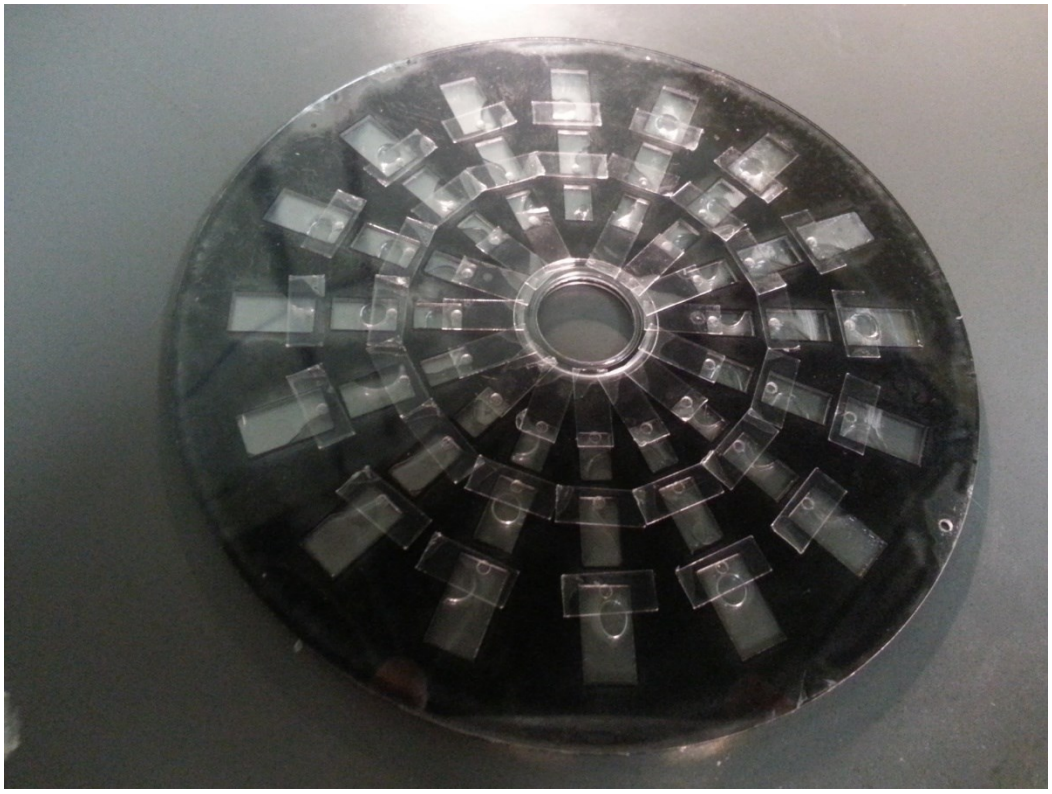

Figure 4-3: Picture of the 1:1.8 aspect ratio test platform following injection of 10 µL aliquots into every chamber.

The effectiveness of the volume measurement technique under varying rotational frequencies was evaluated using the filled rectangular 1:2.3 aspect ratio test platform obtained during the aspect-ratio experiments. Each of the sixteen wedges of this platform was imaged five times for a series of rotational frequencies from 200 to 1400 RPM in 200 RPM increments. Areas for all liquid aliquots were measured and an RSD was computed for aliquots located on the same wedge to obtain RSDs for every rotational frequency.

4.4 Results and Discussion

Artificial platform images obtained at five magnification settings were segmented for eight platform wedges and the area of the 5 mm radius chamber was computed for each wedge. An RSD was then computed for the areas obtained between the different wedges. The results for this magnification study can be found in Table 4-1. As can be seen in this table, the RSD did not present any significant variation with magnification. This demonstrates the robust nature of the segmentation process and the adaptability of the technique across various zoom settings. It is important to note that this study does not take into account the thickness change in the meniscus at low magnifications, which can render segmentation difficult if the background lighting is not of sufficient intensity. Care must be taken to ensure that adequate contrast is provided if imaging at lower magnification is desired.

Table 4-1: Magnification Experiment Data

Magnification	RSD (%)
9.7	1
5.7	1
3.5	1
1.5	2
1	1

To ensure the applicability of the volume measurement technique to coloured liquids, a study was performed using six solutions of food colouring dyes: red, yellow, blue, green, orange and purple. A 50 µL aliquot of each dye was injected into 5 mm radius chambers of a test platform along with a 10 µL calibration aliquot in corresponding 3 mm radius chambers. Each dye aliquot was imaged five times and segmented to obtain an average volume measurement for every colour. The RSD between dye volumes was computed and found to be 1%, indicating that the colour of the analyte did not have any impact on the volume measurement process.

In order to accommodate darker liquid colours, an easy solution can be implemented by modifying the initial grayscale conversion process. Since the white background is uniform in all three colour channels (red, green and blue) for clear-coloured liquids, a specific colour channel can be selected directly instead of using a grayscale conversion algorithm. This selection was automated following a single click inside the coloured liquid aliquot area by the user. A 50 by 50 pixel area was selected around the clicked location and the mean intensity of those pixels was

computed for all three colour planes. The colour channel with the maximum mean intensity was then retained. This ensures that the segmentation occurs on the intensity plane having the highest contrast with the black background which has a value of 0 in every colour channel. The use of a clear calibration aliquot can enable the simultaneous measurement of the volumes of several different coloured analytes in a single image.

To evaluate the effects of surface properties on the precision of the volume measurement technique, an experiment was conducted using four solvents of varying surface tensions: ethylene glycol, hexadecane, methanol and ethanol. A separate test platform was allocated for each solvent. Every chamber of a platform was filled with a 10 µL aliquot of a selected solvent and each wedge was imaged five times while rotating at 1200 RPM. The areas of each aliquot were computed and an RSD for every solvent was calculated between the three aliquots located on the same image in different-sized chambers. While five imaging replicates of each wedge were acquired, some outliers were obtained that failed to segment due to lighting aberrations and were discarded while the areas obtained from the remaining replicates were averaged. The obtained RSDs can be found in Table 4-2 while an example of the images obtained for each solvent can be found in Figure 4-4.

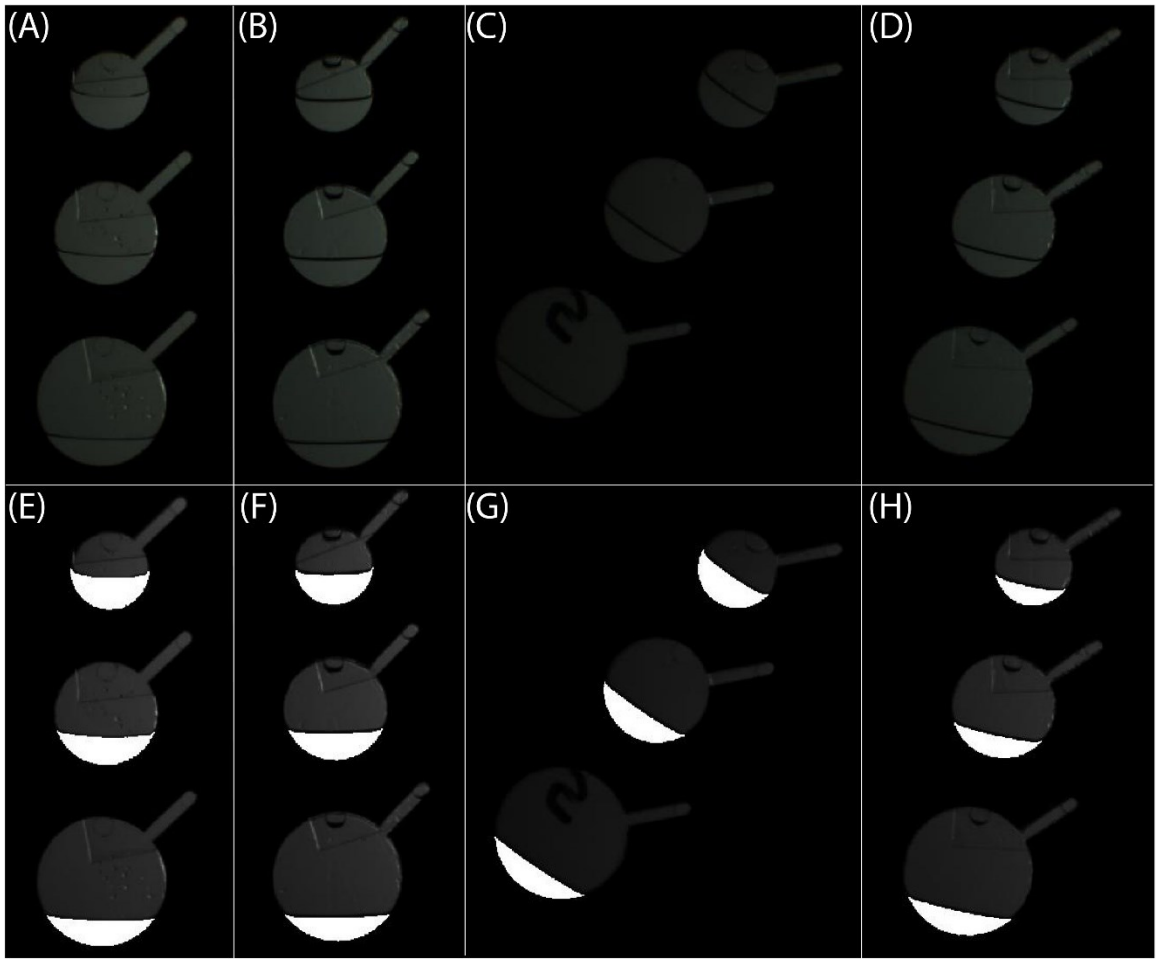

Figure 4-4: Experimental images obtained during the solvent experiment. A) Raw image of ethylene glycol aliquots. B) Raw image of hexadecane aliquots. C) Raw image of methanol aliquots. D) Raw image of ethanol aliquots. E)-H) Images A-D segmented with highlighted aliquot areas.

Table 4-2: Solvent Experiment Data

Solvent	Surface Tension at 25°C (mN/m)[18]	RSD (%)
Ethylene Glycol	47.99	1.00
Hexadecane	27.05	5.00
Methanol	23.23	14.00
Ethanol	23.22	16.00

As can be seen in Table 4-3, method precision was reduced with decreased surface tension of the solvent. The reason for this can be readily observed in the difference in the meniscus between the images for ethylene glycol and hexadecane (Figure 4-4 A-B). As surface tension of the liquid decreases, the contact angle of the meniscus increases. While the meniscus appears flatter in the horizontal domain due to the applied centrifugal force, imaged meniscus thickness increases with surface tension due to the increased wetting of the top and bottom polycarbonate layers. This effect renders segmentation easier due to the thickened meniscus outline. However, it also reduces the precision of area measurements for aliquots of same volume in different-sized chambers since the volume of liquid contained in the meniscus varies with chamber shape.

The precision attained for ethylene glycol matches that of the previously obtained measurements for DDW containing trace amounts of surfactant. The precision difference for methanol and ethanol was significantly larger despite their surface tension being similar to hexadecane. This was most likely caused by interactions between ethanol/methanol and the pressure sensitive adhesive layer of the disk, resulting in leaks at the high RPM at which imaging occurred. The construction materials utilized for our centrifugal microfluidic platform construction severely limited the potential solvents that could be evaluated due to solvent-polycarbonate and solvent-adhesive interactions.

To mitigate the impact of the surface tension of a measured liquid, careful choice of the substrate must be made to reduce wetting of the platform surface by the liquid. However, reduced wetting will result in a thinner meniscus which requires a higher resolution or larger magnification for successful segmentation.

Table 4-3: Aspect Ratio Experiment Data

Chamber Aspect Ratio	RSD
1:1	2%
1:1.8	1%
1:2.3	1%

The effect of chamber shape and aspect ratio on the precision of the volume measurement technique was evaluated using three platforms containing rectangular chambers of varying aspect ratios. A 10 µL aliquot of DDW containing 0.03% of Triton-X was injected into every chamber of a platform with each wedge of the platform being imaged five times. Platform images were segmented and areas were obtained for every aliquot. An RSD between aliquots located on the same image in different sized chambers was computed for every platform. The RSDs obtained can be found in Table 4-3 and example images of each platform are shown in Figure 4-5.

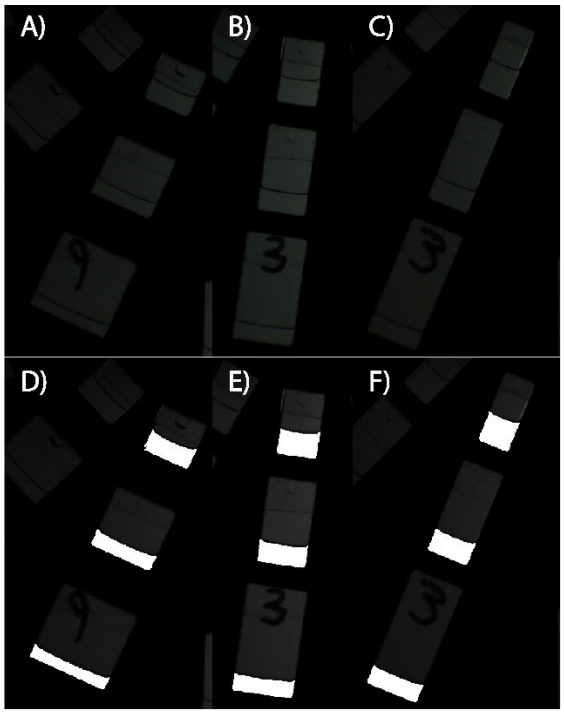

Figure 4-5: Images obtained during the aspect ratio experiments. A) Raw image of the 1:1 aspect ratio platform. B) Raw image of the 1:1.8 aspect ratio platform. C) Raw image of the 1:2.3 aspect ratio platform. D)-F) Images A-C segmented with highlighted aliquot areas.

As can be seen in Table 4-3, the aspect ratio of a rectangular chamber was not found to have any influence on the precision of the volume measurement technique. This indicates that the segmentation of the liquid meniscus shows the same precision as the segmentation of the chamber outline and concurs with measurements obtained in Chapter 3.5 between different chamber sizes where we did not find any correlation between chamber size and RSD. As such, both studies demonstrate that the image segmentation-based technique provides precise volume measurements that can be reliably scaled to chambers of varying size and shape.

A final study was conducted to verify the impact of platform rotational frequency on the precision of volume measurements obtained by image segmentation. The 1:2.3 aspect ratio platform containing 10 µL aliquots of DDW that was utilized in the previous experiment was imaged at various rotational frequencies and an RSD for every frequency was obtained for aliquots located on the same wedge in different sized chambers. The resulting RSDs can be found in Table 4-4 and example images for every frequency are shown in Figure 4-6.

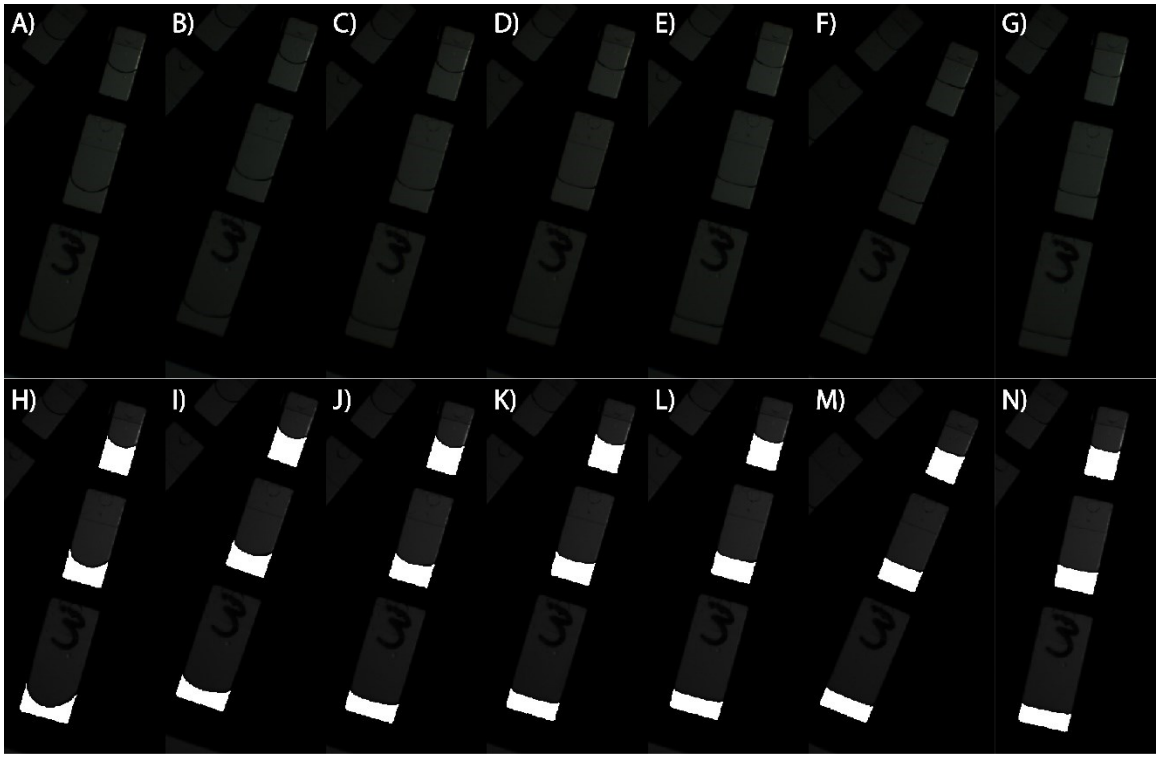

Figure 4-6: Experimental images obtained for aliquots of DDW inside a test platform rotated at A) 200 RPM B) 400 RPM C) 600 RPM D) 800 RPM E) 1000 RPM F) 1200 RPM and G) 1400 RPM. H)-N) Images A-G following segmentation with highlighted aliquot areas.

Table 4-4 : Rotational Frequency	
Rotational Frequency (RPM)	RSD (%)
200	2
400	2
600	2
800	2
1000	2
1200	1
1400	2

The results shown in Table 4-4 indicate that the precision of the obtained area measurements is not affected by rotational frequency. This implies that the curving of the aliquot meniscus on platform images obtained at low rotational frequencies has no effect on the ability of the segmentation process to correctly select liquid outlines for measurements. Flattening of the liquid meniscus at higher rotational frequencies did not provide any advantages in precision. These results further demonstrate the flexibility of the volume measurement technique as it can be reliably applied to platforms under varying rotational frequencies with no loss in precision.

4.5 Conclusion

Image segmentation-based volume measurements were further characterized and the response of the technique to several experimental parameters was analyzed. Experiments have demonstrated that the precision of measurements obtained through this technique is independent of design feature size, aspect ratio,

shape and rotational frequency. A relationship between method precision and the surface tension of a measured liquid was also established. It suggests that solvent effects may be mitigated by an appropriate choice of platform substrate. The developed technique was shown to be a reliable tool for direct measurements of liquid volumes during platform operation and its flexibility for general purpose volume measurements was successfully demonstrated.

4.6 References

1. D. A. Duford, D. D. Peng and E. D. Salin,"Magnetically driven solid sample preparation for centrifugal microfluidic devices", *Analytical chemistry*, **2009**, 81, 4581-4584.

2. M. Grumann, T. Brenner, C. Beer, R. Zengerle and J. Ducrée,"Visualization of flow patterning in high-speed centrifugal microfluidics", *Review of Scientific Instruments*, **2005**, 76, 025101.

3. A. LaCroix-Fralish, J. Clare, C. D. Skinner and E. D. Salin,"A centrifugal microanalysis system for the determination of nitrite and hexavalent chromium", *Talanta*, **2009**, 80, 670-675.

4. M. C. Kong and E. D. Salin,"Spectrophotometric determination of aqueous sulfide on a pneumatically enhanced centrifugal microfluidic platform", *Analytical chemistry*, **2012**, 84, 10038-10043.

5. D. A. Duford, Y. Xi and E. D. Salin,"Enzyme inhibition-based determination of pesticide residues in vegetable and soil in centrifugal microfluidic devices", *Analytical chemistry*, **2013**, 85, 7834-7841.

6. J. Steigert, T. Brenner, M. Grumann, L. Riegger, S. Lutz, R. Zengerle and J. Ducree,"Integrated siphon-based metering and sedimentation of whole blood on a hydrophilic lab-on-a-disk", *Biomed Microdevices*, **2007**, 9, 675-679.

7. J. Steigert, M. Grumann, T. Brenner, L. Riegger, J. Harter, R. Zengerle and J. Ducree,"Fully integrated whole blood testing by real-time absorption measurement on a centrifugal platform", *Lab on a chip*, **2006**, 6, 1040-1044.

8. A. Kazarine, M. C. Kong, E. J. Templeton and E. D. Salin,"Automated liquid-liquid extraction by pneumatic recirculation on a centrifugal microfluidic platform", *Analytical chemistry*, **2012**, 84, 6939-6943.

9. Y. Xi, D. A. Duford and E. D. Salin,"Automated liquid-solid extraction of pyrene from soil on centrifugal microfluidic devices", *Talanta*, **2010**, 82, 1072-1076.

10. D. Mark, T. Metz, S. Haeberle, S. Lutz, J. Ducree, R. Zengerle and F. von Stetten,"Centrifugo-pneumatic valve for metering of highly wetting liquids on centrifugal microfluidic platforms", *Lab on a chip*, **2009**, 9, 3599-3603.

11. D. J. Beebe, G. A. Mensing and G. M. Walker,"Physics and applications of microfluidics in biology", *Annual review of biomedical engineering*, **2002**, 4, 261-286.

12. Y. Yuan and T. R. Lee, in *Surface Science Techniques*, Springer, 2013, pp. 3-34.

13. R. Gorkin, J. Park, J. Siegrist, M. Amasia, B. S. Lee, J. M. Park, J. Kim, H. Kim, M. Madou and Y. K. Cho,"Centrifugal microfluidics for biomedical applications", *Lab on a chip*, **2010**, 10, 1758-1773.

14. M. Madou, J. Zoval, G. Jia, H. Kido, J. Kim and N. Kim,"Lab on a CD", *Annual review of biomedical engineering*, **2006**, 8, 601-628.

15. H. Cho, H.-Y. Kim, J. Y. Kang and T. S. Kim,"How the capillary burst microvalve works", *Journal of colloid and interface science*, **2007**, 306, 379-385.

16. J. Ducree, S. Haeberle, S. Lutz, S. Pausch, F. von Stetten and R. Zengerle,"The centrifugal microfluidic bio-disk platform", *J Micromech Microeng*, **2007**, 17, S103-S115.

17. H. Kido, J. Zoval and M. J. J. Madou,"Rapid Prototyping of Microfludic Systems", **2007**, 4, 101-105.

18. in *CRC Handbook of Chemistry and Physics* ed. D. R. Lide, CRC Press, Internet Version, 94th Edition edn., 2013, pp. 184-185.

5. Conclusions and Future Work

5.1 Conclusions

The goal of this thesis was to establish a non-contact volume measurement technique for liquid aliquots located inside CM platforms in motion. This goal was achieved through the development of a volume measurement technique using the segmentation of platform images acquired in motion.

Measurements obtained by this technique were demonstrated to be:

- Highly reproducible with a relative standard deviation of 1% for clear distilled deionized water aliquots (with 0.03% Triton X).
- Easy to calibrate using pre-metered calibration aliquots located on the same image.
- Applicable to aliquots in chambers of various sizes, shapes and aspect ratios with no loss in precision.
- Flexible in regards to liquid colour.
- Scalable to images acquired at any rotational frequency.
- Lightly affected by the surface tension of measured liquids

In addition, the application of this technique requires minimal user input and does not utilize any instrumentation other than a digital camera and stroboscope, components that are inexpensive and readily available in most CM laboratories where they are utilized for routine qualitative evaluation.

5.2 Summary of thesis work

Chapter 2 presented the instrumentation utilized for the acquisition of high quality platform images in motion and the design and construction of contrast-enhanced CM platforms for method evaluation.

Chapter 3 introduced a digital image processing technique utilized to conduct automatic segmentation of platform images in order to obtain precise volumetric data with minimal user intervention. The figures of merit of the technique were characterized and the potential of the technique for general purpose volume measurements on CM platforms was illustrated.

Chapter 4 offered an extensive characterization of the performance of the volume measurement technique in response to common experimental parameters in order to demonstrate its flexibility towards the needs of experimenters.

5.3 Future work

The groundwork demonstrating the robust capabilities of the image segmentation-based volume measurement technique has been presented in this thesis. Several potential applications of this technique have been envisioned that will enhance the unit operation toolbox available for CM platforms.

The ability to acquire direct volume measurements from platforms in motion could first be applied to the quantitative evaluation of CM platform designs. The

integration of a small calibration chamber on any design should allow for quantitative flow monitoring during platform operation.

The current use of metering chambers in CM platform designs complicates the development of several analytical techniques, which could be overcome through application of the volume measurement technique. A Centrifugal Liquid Addition Distributor (CLAD) device was previously developed in our laboratory[1]. This device allows the non-contact addition of liquids to CM platforms in motion. While capable of providing aliquots as small as 15 µL, the precision of delivery of this device was found to be of around 9% which would require the use of metering chambers for volume calibration. The use of such chambers during continuous liquids addition would then require constant monitoring and manual intervention of experimenters to avoid overflow. This limitation could be easily overcome by measurement of the distributed aliquots through the image segmentation technique. A CM platform utilizing the CLAD could then be developed to conduct the automated spectroscopic determination of several samples in parallel using the method of standards addition. Images obtained before and after addition of a standard aliquot could be used to determine the added volume of standard to each sample without the need for user intervention during device operation or the need for a measurement chamber.

Volumetric titration is a classic analytical technique utilized for the precise determination of compounds. Standard use of this technique requires large quantities of reagents and generates significant waste. While titrations on an electro-osmotic microfluidic platform[2] have been successfully achieved, implementation of volumetric titrations has not been previously attempted on CM platforms due to difficulties in obtaining precise aliquots on this platform. Using the image segmentation-based volumetric measurement technique, a platform could be designed to conduct the automated volumetric titration of samples requiring only the initial injection of the sample, a coloured indicator and a titrant reservoir. Titrant aliquots would then be added using a rapid increase/decrease in rotational frequency and the resulting volume change could be measured through image segmentation. The progress of the titration could be tracked through imaging or spectroscopic methods with the experimenter only needing to determine the end frame from which the final titrated volume would be obtained.

5.4 References

1. A. P. Bouchard, D. A. Duford and E. D. Salin,"Non-contact addition, metering, and distribution of liquids into centrifugal microfluidic devices in motion", *Analytical chemistry*, **2010**, 82, 8386-8389.

2. O. T. Guenat, D. Ghiglione, W. E. Morf and N. F. de Rooij,"Partial electroosmotic pumping in complex capillary systems: Part 2: Fabrication and application of a micro total analysis system (μTAS) suited for continuous volumetric nanotitrations", *Sensors and Actuators B: Chemical*, **2001**, 72, 273-282.

Appendix A: MATLAB GUI

This appendix presents a series of figures depicting the graphic user interface (GUI) developed to implement the volume measurement technique. The GUI was developed using MATLAB. As the GUI was designed to be utilized on high resolution monitors (1920 by 1080 pixels), resizing of figure elements to fit this appendix resulted in a loss of detail. To compensate for this loss, certain parts of the interface were zoomed in and displayed on a separate figure.

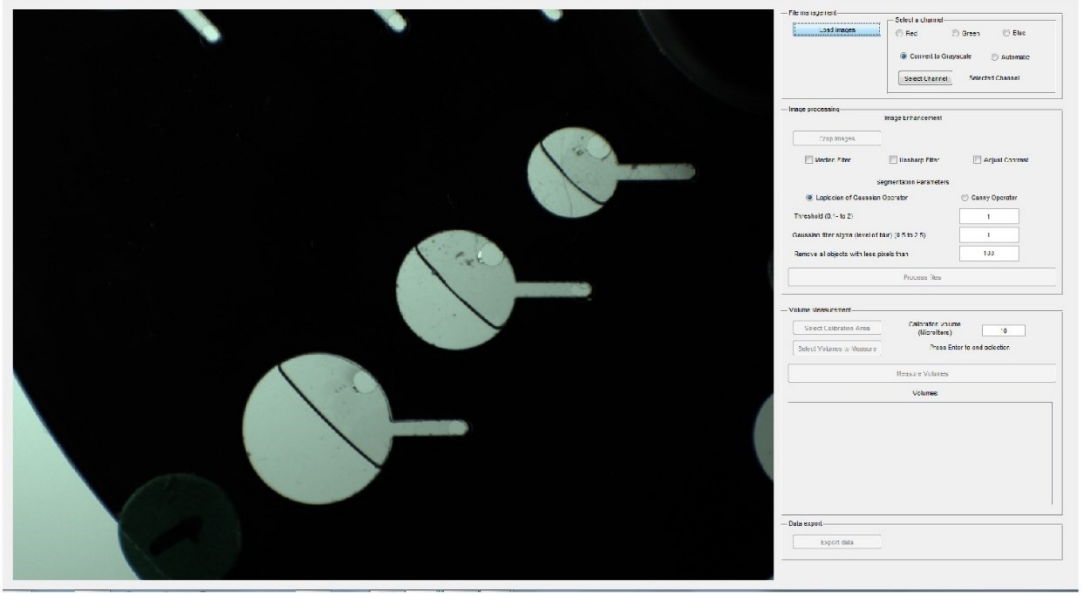

Figure A-1: Loading and display of a set of replicate raw images into the main interface. The first image of the series is displayed.

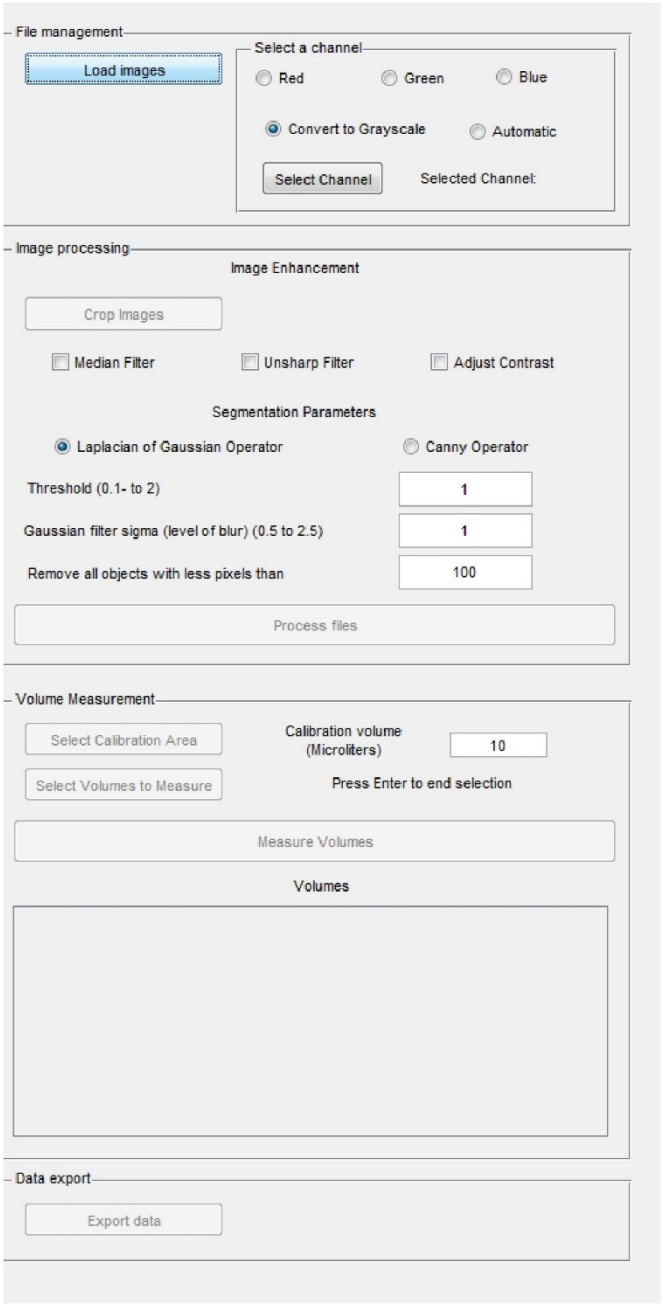

Figure A-2: Zoomed image of the interface depicted on the right of Figure A-1 demonstrating the main menu of the GUI. Following loading of a set of images, conversion to grayscale must be accomplished through one of the methods presented above.

Figure A-3: Conversion and display of raw images into grayscale. The first replicate is displayed following conversion.

Figure A-4: Segmentation of grayscale images. All images are segmented using the selected settings and the first replicate is then displayed.

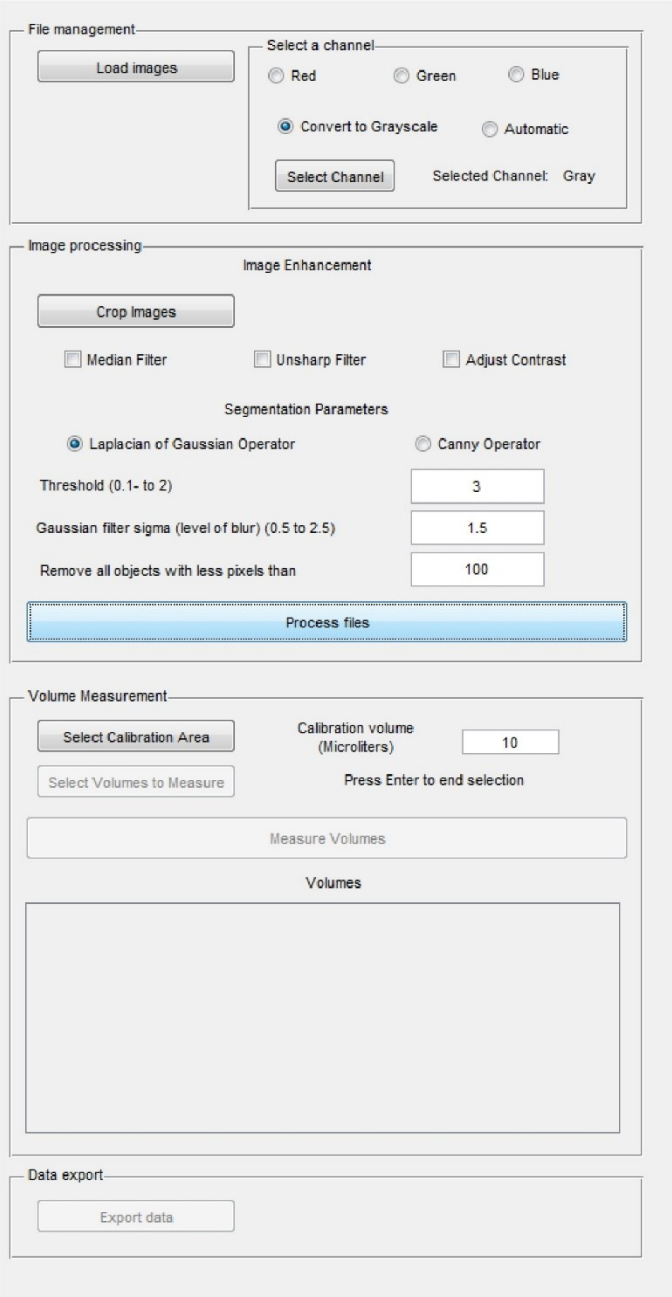

Figure A-5: Zoomed image of the interface depicted on the right of Figure A-4 demonstrating the main menu of the GUI. Segmentation parameters are modified by the user for optimal segmentation. The threshold parameter multiplies the automatically-generated threshold by the user entered number. Here, the default threshold is multiplied by 3 rendering the edge-selection process more selective. The standard deviation of the Gaussian component of the Laplacian-of-Gaussian operator is then selected. Finally, a cleanup is performed for segmented objects that are below a certain pixel limit which is specified by the user.

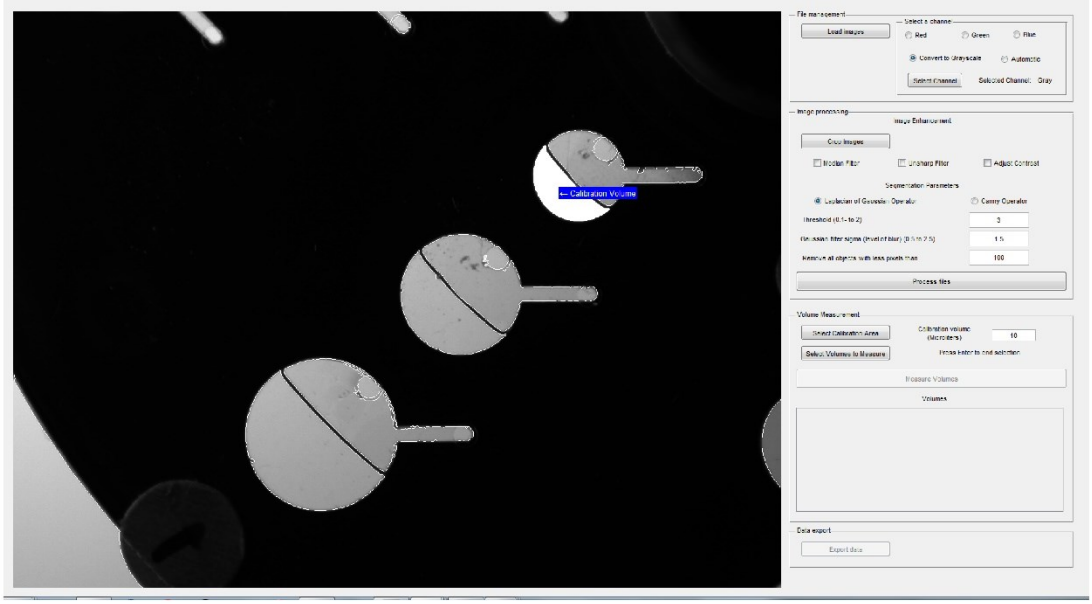

Figure A-6: Selection of the calibration volume by the user. The same coordinates are applied to all replicate images of a set.

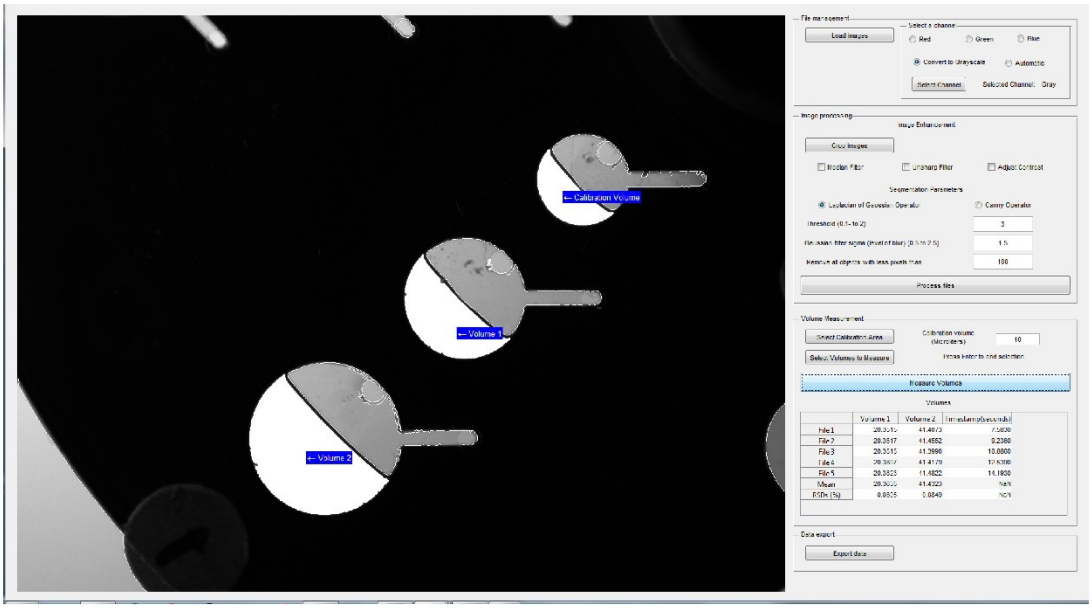

Figure A-7: Selection of the aliquots to measure by the user. The same coordinates are applied to all replicate images of a set. The measure button is then pressed to obtain the volume measurements.

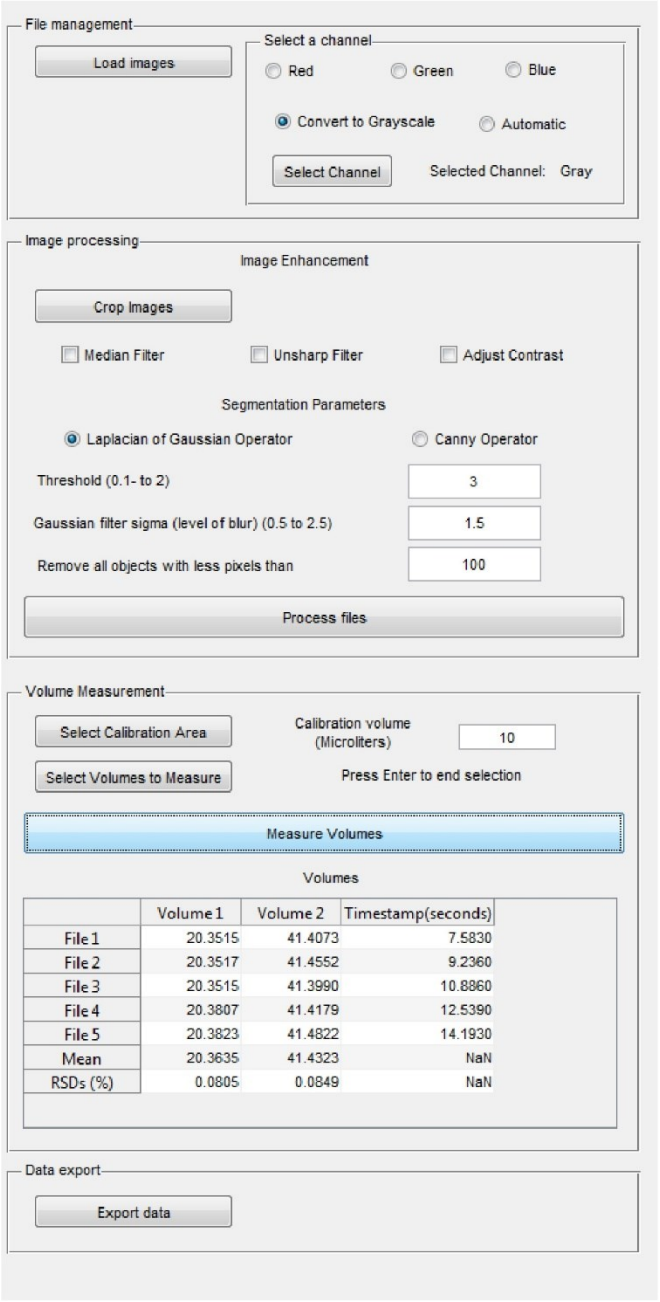

Figure A-8: Zoomed image of the interface depicted on the right of Figure A-7 demonstrating the main menu of the GUI. The volume of the calibration aliquot is entered by the user with the default being 10. The volume for each aliquot is then calculated and presented to the user for each file. Replicate statistics and the timestamp of each image are then presented for convenience.